Study of π^{0} pair production in single-tag two-photon collisions

M. Masuda *et al.* (The Belle Collaboration)

Phys. Rev. D **93**, 032003 — Published 18 February 2016

DOI: 10.1103/PhysRevD.93.032003

Study of π^0 pair production in single-tag two-photon collisions

M. Masuda,[69] S. Uehara,[15,11] Y. Watanabe,[27] H. Nakazawa,[47] A. Abdesselam,[63] I. Adachi,[15,11] H. Aihara,[70] S. Al Said,[63,31] D. M. Asner,[55] H. Atmacan,[41] V. Aulchenko,[4,53] T. Aushev,[43,25] V. Babu,[64] I. Badhrees,[63,30] A. M. Bakich,[62] E. Barberio,[40] P. Behera,[19] B. Bhuyan,[18] J. Biswal,[26] A. Bobrov,[4,53] G. Bonvicini,[76] A. Bozek,[50] M. Bračko,[38,26] T. E. Browder,[14] D. Červenkov,[5] V. Chekelian,[39] A. Chen,[47] B. G. Cheon,[13] K. Chilikin,[25] R. Chistov,[25] K. Cho,[32] V. Chobanova,[39] S.-K. Choi,[12] Y. Choi,[61] D. Cinabro,[76] J. Dalseno,[39,65] M. Danilov,[25,42] N. Dash,[17] J. Dingfelder,[3] Z. Doležal,[5] Z. Drásal,[5] D. Dutta,[64] S. Eidelman,[4,53] D. Epifanov,[70] H. Farhat,[76] J. E. Fast,[55] T. Ferber,[8] B. G. Fulsom,[55] V. Gaur,[64] N. Gabyshev,[4,53] A. Garmash,[4,53] R. Gillard,[76] F. Giordano,[79] R. Glattauer,[22] Y. M. Goh,[13] P. Goldenzweig,[28] B. Golob,[36,26] J. Haba,[15,11] K. Hayasaka,[45] H. Hayashii,[46] X. H. He,[56] W.-S. Hou,[49] T. Iijima,[45,44] K. Inami,[44] A. Ishikawa,[68] R. Itoh,[15,11] Y. Iwasaki,[15] I. Jaegle,[14] D. Joffe,[29] K. K. Joo,[6] T. Julius,[40] K. H. Kang,[34] E. Kato,[68] T. Kawasaki,[52] D. Y. Kim,[60] J. B. Kim,[33] J. H. Kim,[32] K. T. Kim,[33] M. J. Kim,[34] S. H. Kim,[13] Y. J. Kim,[32] B. R. Ko,[33] S. Korpar,[38,26] P. Križan,[36,26] P. Krokovny,[4,53] T. Kumita,[72] A. Kuzmin,[4,53] Y.-J. Kwon,[78] J. S. Lange,[9] D. H. Lee,[33] I. S. Lee,[13] C. Li,[40] L. Li,[58] Y. Li,[75] J. Libby,[19] D. Liventsev,[75,15] P. Lukin,[4,53] D. Matvienko,[4,53] K. Miyabayashi,[46] H. Miyata,[52] R. Mizuk,[25,42] G. B. Mohanty,[64] S. Mohanty,[64,74] A. Moll,[39,65] H. K. Moon,[33] T. Mori,[44] R. Mussa,[24] E. Nakano,[54] M. Nakao,[15,11] T. Nanut,[26] Z. Natkaniec,[50] M. Nayak,[19] N. K. Nisar,[64] S. Nishida,[15,11] S. Ogawa,[67] P. Pakhlov,[25,42] G. Pakhlova,[43,25] B. Pal,[7] C. W. Park,[61] H. Park,[34] T. K. Pedlar,[37] R. Pestotnik,[26] M. Petrič,[26] L. E. Piilonen,[75] J. Rauch,[66] E. Ribežl,[26] M. Ritter,[39] A. Rostomyan,[8] S. Sandilya,[64] L. Santelj,[15] T. Sanuki,[68] Y. Sato,[44] V. Savinov,[57] O. Schneider,[35] G. Schnell,[1,16] C. Schwanda,[22] Y. Seino,[52] K. Senyo,[77] O. Seon,[44] M. E. Sevior,[40] V. Shebalin,[4,53] C. P. Shen,[2] T.-A. Shibata,[71] J.-G. Shiu,[49] B. Shwartz,[4,53] F. Simon,[39,65] Y.-S. Sohn,[78] A. Sokolov,[23] E. Solovieva,[25] M. Starič,[26] M. Sumihama,[10] T. Sumiyoshi,[72] U. Tamponi,[24,73] K. Tanida,[59] Y. Teramoto,[54] T. Uglov,[25,43] Y. Unno,[13] S. Uno,[15,11] C. Van Hulse,[1] P. Vanhoefer,[39] G. Varner,[14] A. Vinokurova,[4,53] V. Vorobyev,[4,53] A. Vossen,[20] M. N. Wagner,[9] C. H. Wang,[48] M.-Z. Wang,[49] P. Wang,[21] K. M. Williams,[75] E. Won,[33] J. Yamaoka,[55] Y. Yamashita,[51] S. Yashchenko,[8] H. Ye,[8] Y. Yusa,[52] C. C. Zhang,[21] Z. P. Zhang,[58] V. Zhilich,[4,53] V. Zhulanov,[4,53] and A. Zupanc[26]

(The Belle Collaboration)

[1] *University of the Basque Country UPV/EHU, 48080 Bilbao*
[2] *Beihang University, Beijing 100191*
[3] *University of Bonn, 53115 Bonn*
[4] *Budker Institute of Nuclear Physics SB RAS, Novosibirsk 630090*
[5] *Faculty of Mathematics and Physics, Charles University, 121 16 Prague*
[6] *Chonnam National University, Kwangju 660-701*
[7] *University of Cincinnati, Cincinnati, Ohio 45221*
[8] *Deutsches Elektronen–Synchrotron, 22607 Hamburg*
[9] *Justus-Liebig-Universität Gießen, 35392 Gießen*
[10] *Gifu University, Gifu 501-1193*
[11] *SOKENDAI (The Graduate University for Advanced Studies), Hayama 240-0193*
[12] *Gyeongsang National University, Chinju 660-701*
[13] *Hanyang University, Seoul 133-791*
[14] *University of Hawaii, Honolulu, Hawaii 96822*
[15] *High Energy Accelerator Research Organization (KEK), Tsukuba 305-0801*
[16] *IKERBASQUE, Basque Foundation for Science, 48013 Bilbao*
[17] *Indian Institute of Technology Bhubaneswar, Satya Nagar 751007*
[18] *Indian Institute of Technology Guwahati, Assam 781039*
[19] *Indian Institute of Technology Madras, Chennai 600036*
[20] *Indiana University, Bloomington, Indiana 47408*
[21] *Institute of High Energy Physics, Chinese Academy of Sciences, Beijing 100049*
[22] *Institute of High Energy Physics, Vienna 1050*

[23]*Institute for High Energy Physics, Protvino 142281*
[24]*INFN - Sezione di Torino, 10125 Torino*
[25]*Institute for Theoretical and Experimental Physics, Moscow 117218*
[26]*J. Stefan Institute, 1000 Ljubljana*
[27]*Kanagawa University, Yokohama 221-8686*
[28]*Institut für Experimentelle Kernphysik, Karlsruher Institut für Technologie, 76131 Karlsruhe*
[29]*Kennesaw State University, Kennesaw GA 30144*
[30]*King Abdulaziz City for Science and Technology, Riyadh 11442*
[31]*Department of Physics, Faculty of Science, King Abdulaziz University, Jeddah 21589*
[32]*Korea Institute of Science and Technology Information, Daejeon 305-806*
[33]*Korea University, Seoul 136-713*
[34]*Kyungpook National University, Daegu 702-701*
[35]*École Polytechnique Fédérale de Lausanne (EPFL), Lausanne 1015*
[36]*Faculty of Mathematics and Physics, University of Ljubljana, 1000 Ljubljana*
[37]*Luther College, Decorah, Iowa 52101*
[38]*University of Maribor, 2000 Maribor*
[39]*Max-Planck-Institut für Physik, 80805 München*
[40]*School of Physics, University of Melbourne, Victoria 3010*
[41]*Middle East Technical University, 06531 Ankara*
[42]*Moscow Physical Engineering Institute, Moscow 115409*
[43]*Moscow Institute of Physics and Technology, Moscow Region 141700*
[44]*Graduate School of Science, Nagoya University, Nagoya 464-8602*
[45]*Kobayashi-Maskawa Institute, Nagoya University, Nagoya 464-8602*
[46]*Nara Women's University, Nara 630-8506*
[47]*National Central University, Chung-li 32054*
[48]*National United University, Miao Li 36003*
[49]*Department of Physics, National Taiwan University, Taipei 10617*
[50]*H. Niewodniczanski Institute of Nuclear Physics, Krakow 31-342*
[51]*Nippon Dental University, Niigata 951-8580*
[52]*Niigata University, Niigata 950-2181*
[53]*Novosibirsk State University, Novosibirsk 630090*
[54]*Osaka City University, Osaka 558-8585*
[55]*Pacific Northwest National Laboratory, Richland, Washington 99352*
[56]*Peking University, Beijing 100871*
[57]*University of Pittsburgh, Pittsburgh, Pennsylvania 15260*
[58]*University of Science and Technology of China, Hefei 230026*
[59]*Seoul National University, Seoul 151-742*
[60]*Soongsil University, Seoul 156-743*
[61]*Sungkyunkwan University, Suwon 440-746*
[62]*School of Physics, University of Sydney, NSW 2006*
[63]*Department of Physics, Faculty of Science, University of Tabuk, Tabuk 71451*
[64]*Tata Institute of Fundamental Research, Mumbai 400005*
[65]*Excellence Cluster Universe, Technische Universität München, 85748 Garching*
[66]*Department of Physics, Technische Universität München, 85748 Garching*
[67]*Toho University, Funabashi 274-8510*
[68]*Tohoku University, Sendai 980-8578*
[69]*Earthquake Research Institute, University of Tokyo, Tokyo 113-0032*
[70]*Department of Physics, University of Tokyo, Tokyo 113-0033*
[71]*Tokyo Institute of Technology, Tokyo 152-8550*
[72]*Tokyo Metropolitan University, Tokyo 192-0397*
[73]*University of Torino, 10124 Torino*
[74]*Utkal University, Bhubaneswar 751004*
[75]*CNP, Virginia Polytechnic Institute and State University, Blacksburg, Virginia 24061*
[76]*Wayne State University, Detroit, Michigan 48202*
[77]*Yamagata University, Yamagata 990-8560*
[78]*Yonsei University, Seoul 120-749*
[79]*University of Illinois at Urbana-Champaign, Urbana, Illinois 61801*

We report a measurement of the differential cross section of π^0 pair production in single-tag two-photon collisions, $\gamma^*\gamma \to \pi^0\pi^0$, in e^+e^- scattering. The cross section is measured for Q^2

up to 30 GeV^2, where Q^2 is the negative of the invariant mass squared of the tagged photon, in the kinematic range 0.5 GeV $< W <$ 2.1 GeV and $|\cos\theta^*| < 1.0$ for the total energy and pion scattering angle, respectively, in the $\gamma^*\gamma$ center-of-mass system. The results are based on a data sample of 759 fb^{-1} collected with the Belle detector at the KEKB asymmetric-energy e^+e^- collider. The transition form factor of the $f_0(980)$ and that of the $f_2(1270)$ with the helicity-0, -1, and -2 components separately are measured for the first time and are compared with theoretical calculations.

PACS numbers: 12.38.Qk, 13.40.Gp, 14.40.Be, 13.60.Le, 13.66.Bc

I. INTRODUCTION

Single-tag two-photon production of a C-even hadronic system ($\mathcal{M}$), $\gamma^*\gamma \to \mathcal{M}$, is an important reaction to investigate the nature of strong interactions in the low energy region, where perturbative Quantum Chromodynamics (QCD) cannot be applied. It also provides valuable information on the Q^2 dependence of the transition form factor (TFF), where Q^2 is the negative of the invariant mass squared of the tagged photon. This reaction can be studied through the process of $e^+e^- \to e^\pm(e^\mp)\mathcal{M}$, where $(e^\mp)$ indicates an undetected electron or positron, and results of the measurement can be directly compared to QCD-based theoretical predictions. Diehl, Gousset and Pire considered this process at large Q^2 and small W (< 1 GeV) in terms of constituent-hard scattering and generalized distribution amplitudes and predicted a sizable cross section at LEP and B factories [1]; it is indeed the case at a B factory as reported here. Based on this framework, Braun and Kivel pointed out that the measurement of the TFF of the $f_2(1270)$ will be useful to cleanly determine a gluon admixture in tensor mesons at large enough Q^2 [2]. In addition, a data-driven dispersive approach was suggested recently [3], allowing a more precise estimate of the hadronic light-by-light contribution to the anomalous magnetic moment of the muon $(g-2)$.

Schuler, Berends, and van Gulik, who had calculated meson TFFs based on a heavy quark approximation [4], found that their calculations apply well to light mesons as well with only minor modifications. The predicted Q^2 dependence of TFFs for mesons with $J^{PC} = 0^{++}$ and 2^{++} is summarized in Table I, where the $\gamma^*\gamma$ center-of-mass (c.m.) energy W is replaced by the resonance mass M and λ represents the total helicity of the two incident photons. Note that the helicity-1 ($\lambda = 1$) state is allowed when a photon is off the mass shell. According to Table I, TFFs for the helicity-0 and -1 components of a tensor meson grow with Q^2, a prediction which is amenable to investigation.

TABLE I: Predicted Q^2 dependence of transition form factors of mesons for various helicities λ of two incident photons [4]. Each term has a common divisor of $(1 + Q^2/M^2)^2$.

J^{PC}	Q^2 dependence $\left(\div\left(1+\frac{Q^2}{M^2}\right)^2\right)$		
	$\lambda = 0$	$\lambda = 1$	$\lambda = 2$
0^{++}	$\left(1+\frac{Q^2}{3M^2}\right)$	–	–
2^{++}	$\frac{Q^2}{\sqrt{6}M^2}$	$\frac{\sqrt{Q^2}}{\sqrt{2}M}$	1

Recently, Pascalutsa, Pauk, and Vanderhaeghen have formulated sum rules for $\gamma^*\gamma^*$ fusion cross sections, finding several new exact superconvergence relations that are integrated to zero [5]. They derive two predictions for the helicity-2 TFF of the $f_2(1270)$ from two sum rules in the case of one virtual and one real photon under the assumption that the sum rules are saturated by low mass resonances including the $f_2(1270)$. In one sum rule, the integrand has contributions from pseudoscalar mesons and tensor mesons. In the other, axial-vector mesons and tensor mesons contribute to its integrand. The first (second) sum rule gives the helicity-2 TFF of the $f_2(1270)$ in terms of TFF information of the η and η' ($f_1(1285)$ and $f_1(1420)$). With pseudoscalar (P) mesons, the helicity-2 TFF of the $f_2(1270)$ is given by

$$F_{f_2}(Q^2) = \sqrt{\frac{f}{\left(1+\frac{Q^2}{\Lambda_\eta^2}\right)^2} + \frac{1-f}{\left(1+\frac{Q^2}{\Lambda_{\eta'}^2}\right)^2}}\,, \qquad (1)$$

where Λ_η and $\Lambda_{\eta'}$ are the pole masses and $f = c_\eta/(c_\eta + c_{\eta'})$, with $c_P = \Gamma_{\gamma\gamma}(P)/m_P^3$. The relevant parameters are summarized in Table II. In another sum rule for axial-vector (A) mesons, the helicity-2

TABLE II: Parameters of the η, η' [6], $f_1(1285)$, and $f_1(1420)$ [7, 8]. $\Gamma_{\gamma\gamma}$ for an axial-vector meson shall read $\tilde{\Gamma}_{\gamma\gamma}$ defined in Eq. (3).

Meson	$M_M(\mathrm{MeV}/c^2)$	$\Gamma_{\gamma\gamma}(\mathrm{keV})$	$\Lambda_M(\mathrm{MeV}/c^2)$
η	547.853 ± 0.024	0.510 ± 0.026	774 ± 29
η'	957.78 ± 0.06	4.29 ± 0.14	859 ± 28
$f_1(1285)$	1281.8 ± 0.6	3.5 ± 0.8	1040 ± 78
$f_1(1420)$	1426.4 ± 0.9	3.2 ± 0.9	926 ± 78

TFF of the $f_2(1270)$ is given by

$$F_{f_2}(Q^2) = \left(1+\frac{Q^2}{m_{f_2}^2}\right)^{\frac{1}{2}} \times \sqrt{\frac{f}{\left(1+\frac{Q^2}{\Lambda_{f_1}^2}\right)^4}+\frac{1-f}{\left(1+\frac{Q^2}{\Lambda_{f_1'}^2}\right)^4}}\,, \quad (2)$$

where Λ_{f_1} and $\Lambda_{f_1'}$ are the pole masses and $f = c_{f_1}/(c_{f_1}+c_{f_1'})$, with $c_A = 3\tilde{\Gamma}_{\gamma\gamma}(A)/m_A^5$. The effective two-photon width of the A resonance is defined as

$$\tilde{\Gamma}_{\gamma\gamma}(A) = \lim_{Q^2\to 0}\frac{M_A^2}{Q^2}\Gamma(A\to\gamma_L^*\gamma_T), \quad (3)$$

where $\Gamma(A\to\gamma_L^*\gamma_T)$ is the parameter of the axial-vector meson A decaying into a virtual longitudinal photon and a real transverse photon. The relevant parameters are also summarized in Table II.

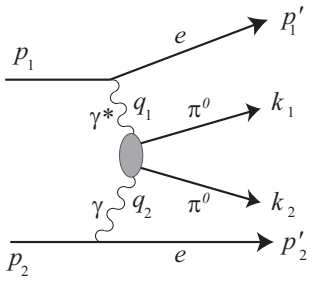

FIG. 1: Feynman diagram for the process $e^+e^- \to e(e)\pi^0\pi^0$. p_1, p_1', p_2, and p_2' are the four-momenta of the incident and scattered electron or positron, q_1, q_2 are those of the virtual and real photons and k_1, k_2 are those of the produced π^0 mesons.

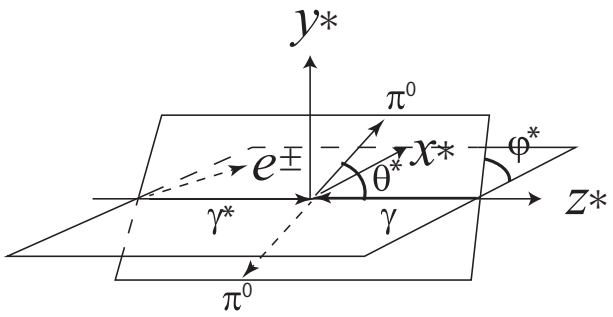

FIG. 2: Definition of the coordinate system for $\gamma^*\gamma \to \pi^0\pi^0$. The incident γ^* and γ are along the z^* axis, the tagged $e^\pm$ is in the x^*z^* plane with $p_{x^*\mathrm{tag}} > 0$, and a π^0 is produced at angles (θ^*, φ^*).

Experimentally, for pseudoscalar mesons, the TFF of the π^0 meson has been measured recently by BaBar [9] and by Belle [10], and those of η and η' [11] and η_c [12] by BaBar for $Q^2 \le 40$ GeV^2.

Two-photon production of axial-vector mesons, $f_1(1285)$ and $f_1(1420)$, which is interpreted as a two-photon fusion of a longitudinal (helicity-0) and a real photon, was studied by the L3 collaboration, who measured the parameters listed in Table II [7, 8]. For scalar or tensor mesons, no significant data for the high-Q^2 region beyond the ρ-meson mass scale exist to be compared with QCD predictions; only yields consistent with zero were reported for $\gamma^*\gamma \to f_2(1270) \to \pi^+\pi^-$ at $Q^2 > 1.0$ GeV^2 by the TPC/Two-Gamma collaboration [13].

We report a measurement of the process $e^+e^- \to e(e)\pi^0\pi^0$, where one of the $e^\pm$ is detected together with $\pi^0\pi^0$ while the other $e^\mp$ is scattered in the forward direction and undetected. The Feynman diagram for the process is shown in Fig. 1, where the four-momenta of the particles are defined. We consider the process $\gamma^*\gamma \to \pi^0\pi^0$ in the c.m. system of the $\gamma^*\gamma$. We define the $x^*y^*z^*$-coordinate system as shown in Fig. 2 at fixed values of W and Q^2; the asterisks here denote the coordinate system that is used for angular variables for the differential cross sections. One of the π^0 mesons is scattered at angles (θ^*, φ^*). Because of the identical particles in the final state and P symmetry in the reaction, only the region where $\theta^* \le \pi/2$ and $0 \le \varphi^* \le \pi$ is meaningful. The z^*-axis is along the incident γ^* and the x^*z^* plane is defined by the tagged $e^\pm$ such that $p_{x^*\,\mathrm{tag}} > 0$, where $\boldsymbol{p}_{\mathrm{tag}}$ is the 3-momentum of the tagged $e^\pm$.

The differential cross section for $\gamma^*\gamma \to \pi^0\pi^0$ is given by [14]

$$\frac{d\sigma(\gamma^*\gamma\to\pi^0\pi^0)}{d\Omega} = \sum_{n=0}^{2} t_n \cos(n\varphi^*), \quad (4)$$

with

$$t_0 = |M_{++}|^2 + |M_{+-}|^2 + 2\epsilon_0|M_{0+}|^2, \quad (5)$$
$$t_1 = 2\epsilon_1 \Re\left((M^*_{+-} - M^*_{++})M_{0+}\right), \quad (6)$$
$$t_2 = -2\epsilon_0 \Re(M^*_{+-}M_{++}). \quad (7)$$

Here, M_{++}, M_{0+}, and M_{+-} are helicity amplitudes whose subscripts $+$, $-$, and 0 indicate the helicity state of the incident virtual photon along, opposite, and transverse to the quantization axis, respectively, and ϵ_0 and ϵ_1 are given by

$$\epsilon_0 = \frac{1-x}{1-x+\frac{x^2}{2}}, \quad (8)$$
$$\epsilon_1 = \frac{(2-x)\sqrt{\frac{(1-x)}{2}}}{1-x+\frac{x^2}{2}}. \quad (9)$$

In turn, x is defined as

$$x = \frac{(q_1 \cdot q_2)}{(p_1 \cdot q_2)}, \quad (10)$$

where q_1, q_2, p_1, and p_2 are the four-momenta of the virtual and real photons and the incident electron and positron, respectively, as defined in Fig. 1. When Eq. (4) is integrated over φ^*, we obtain

$$\frac{d\sigma(\gamma^*\gamma \to \pi^0\pi^0)}{4\pi d|\cos\theta^*|} = |M_{++}|^2 + |M_{+-}|^2 + 2\epsilon_0|M_{0+}|^2. \quad (11)$$

The total cross section is obtained by integrating Eq. (11) over $\cos\theta^*$. It can be written as

$$\sigma_{\rm tot}(\gamma^*\gamma \to \pi^0\pi^0) = \sigma_{TT} + \epsilon_0\sigma_{LT}, \quad (12)$$

where σ_{TT} (σ_{LT}) corresponds to the total cross section of two photons, both of which are transversely polarized (one transversely and the other longitudinally polarized); as $Q^2 \to 0$, the second term vanishes and σ_{TT} approaches the total cross section of real photon-photon scattering.

Neutral-pion pair production in the final state $e(e)\pi^0\pi^0$ is different from the corresponding charged-pair process, $e(e)\pi^+\pi^-$: the $\pi^0\pi^0$ is a pure C-even state, whereas the $\pi^+\pi^-$ is a mixture of C-even and C-odd states. Thus, the $\pi^0\pi^0$ state has no contribution from single-photon production ("bremsstrahlung process"), whose effect must be considered in two-photon production of $\pi^+\pi^-$.

In this paper, we report for the first time a measurement of the cross section for the process $\gamma^*\gamma \to \pi^0\pi^0$ up to $Q^2 = 30\ {\rm GeV}^2$, from which we extract the TFF of the $f_0(980)$ and helicity-0, -1, and -2 TFFs of the $f_2(1270)$.

This article is organized as follows. Section II briefly describes the Belle detector and the data sample used in this measurement. The Monte Carlo (MC) program used for producing simulated events and for efficiency determination is described in Sec. III. Selection of events and comparison with MC data are explained in Sec. IV. Section V is devoted to estimation of possible backgrounds. The differential cross section is derived and its systematic uncertainties are estimated in Sec. VI. In Sec. VII, the cross section is parameterized and fitted to extract the TFFs of the $f_0(980)$ and the helicity-0, -1, and -2 components of the $f_2(1270)$ as a function of Q^2, which are compared to theoretical predictions. Finally, Sec. VIII provides the summary and conclusion.

II. EXPERIMENTAL APPARATUS AND DATA SAMPLE

In this section, we briefly describe the Belle detector and the data sample. We use a 759 fb^{-1} data sample recorded with the Belle detector [15, 16] at the KEKB asymmetric-energy e^+e^- collider [17]. We combine data samples collected at several beam energies: at the $\Upsilon(4S)$ resonance ($\sqrt{s} = 10.58$ GeV), where the beam energy for the electron (positron) beam is 8 GeV (3.5 GeV), and 60 MeV below it (637 fb^{-1} in total); at the $\Upsilon(3S)$ resonance ($\sqrt{s} =$ 10.36 GeV, 3.2 fb^{-1}); and near the $\Upsilon(5S)$ resonance ($\sqrt{s} = 10.88$ GeV, 119 fb^{-1}). Correspondingly, when combining the data, the slight dependence of the two-photon cross section on beam energy is taken into account as described in Sec. VI.

This analysis is performed in the "single-tag" mode, where either the recoil electron or positron (hereinafter referred to as an electron) alone is detected. As described in Sec. IV in more detail, we restrict the virtuality (Q^2) of the untagged-side photon to be small by imposing a strict transverse-momentum balance between the tagged electron and the final-state neutral pion pair in the e^+e^- c.m. frame with respect to the beam axis. In this article, we refer to events tagged by an e^+ or an e^- as "p-tag" (positron-tag) or "e-tag" (electron-tag), respectively.

A. Belle detector

A comprehensive description of the Belle detector is given elsewhere [15, 16]. In the following, we describe only the detector components essential for this measurement. Charged tracks are reconstructed

from the drift-time information in a central drift chamber (CDC) located in a uniform 1.5 T solenoidal magnetic field. The z axis of the detector and the solenoid is along the positron beam direction, with the positron beam pointing in the $-z$ direction. The electron-beam direction at the collision point is 22 mrad from the z axis. The CDC measures the longitudinal and transverse momentum components, *i.e.*, along the z axis and in the $r\varphi$ plane perpendicular to the beam, respectively. Track trajectory coordinates near the collision point are provided by a silicon vertex detector. Photon detection and energy measurements are performed with a CsI(Tl) electromagnetic calorimeter (ECL) by clustering of the energy deposits in the crystals of the electromagnetic shower from an energetic photon, where a possible connection of a charged track to the cluster is examined by extrapolating the track trajectory. Electron identification (ID) is based on E/p, the ratio of the calorimeter energy to the track momentum.

B. Data sample

To be recorded, events of interest here must satisfy one of the two ECL-based triggers: the HiE (High-energy threshold) trigger and the Clst4 (four-energy-cluster) trigger [18].

The HiE trigger requires that the sum of the energies measured by the ECL in an event exceed 1.15 GeV but that the event be not Bhabha-like; the latter requirement is enforced by the absence of the CsiBB trigger ("Bhabha-veto"), which is designed to identify back-to-back Bhabha events [18]. For the purpose of monitoring trigger performance, we record one in 50 events that satisfy the CsiBB trigger (*i.e.*, prescaled by a factor of 50).

The Clst4 trigger requires at least four energy clusters in the ECL with each cluster energy larger than 0.11 GeV. This trigger is not vetoed by the CsiBB because the Bhabha-event rate is manageable for the Clst4 trigger sample. Five clusters are expected in total in the signal events of interest if all the final-state particles are detected in the region where the ECL trigger is sensitive.

We do not use information from the charged-track triggers because they require two or more charged tracks whereas our signal has only one.

III. SIGNAL MONTE CARLO CODE

A. Signal Monte Carlo, TREPSBSS

We use the signal Monte Carlo (MC) generator TREPSBSS, which has been developed to calculate the efficiency for single-tag two-photon events, $e^+e^- \to e(e)X$, as well as the two-photon luminosity function for $\gamma^*\gamma$ collisions at an e^+e^- collider.

TREPSBSS implements Eqs. (2.16) to (2.20) of Ref. [19] and is based on the MC code in Ref. [20], which was modified to match the single-tag configuration. We regard Eq. (12) as the total cross section of the $\gamma^*\gamma$ collisions, according to Eq. (2.16) of Ref. [19], although ϵ_0 is a variable depending on experimental conditions. It is possible to estimate ϵ_0 for specific experimental conditions by taking the average value of ϵ_0 calculated for the selected signal events in MC or experimental data. Under our experimental conditions, ϵ_0 ranges from 0.7 to 0.9. However, $\sigma_{\rm LT}$ cannot be separated from $\sigma_{\rm TT}$ based on this information only.

In TREPSBSS, the following kinematical variables are used for characterizing $\gamma^*\gamma$ collisions of the generated events and for an integration to calculate the two-photon luminosity function: Q_1^2 and Q_2^2 (the absolute value of momentum transfer squared of the highly virtual and the less virtual incident photons, respectively), W (c.m. energy of the incident $\gamma^*\gamma$ system), ω_2 (the energy of the photon with the smaller virtuality), and $\Delta\varphi$ (the azimuthal-angle difference between the two virtual photons). The choice of kinematical variables is discussed in Ref. [21].

We always retain the condition $Q_1^2 > Q_2^2$ for the virtuality of the two colliding photons by requiring $Q_1^2 > 3.0$ GeV^2 and $Q_2^2 < 1.0$ GeV^2 for the ranges of integration, event generation, and selection. This Q_2^2 range is sufficient to generate signal events over the kinematical region for the $|\Sigma \boldsymbol{p}_t^*|$ selection criterion.

The form-factor effect for the photon with the smaller virtuality is assumed to follow the $1/(1 + Q_2^2/m_\rho^2)^2$ dependence, where m_ρ is the ρ-meson mass, 0.77 GeV/c^2. The cross section defined below is that extrapolated to $Q_2^2 = 0$, assuming this Q_2^2 dependence.

The distribution of Q_1^2 ($\equiv Q^2$) in the MC sample is arbitrary and should not affect the final result. Conventionally, we choose the distribution corresponding to the flat form factor in order to retain high statistics of the signal MC in the high-Q^2 region but we weight the MC sample by an additional $1/Q^2$ factor to model a more realistic distribution for the efficiency derivation in each Q^2 region discussed in this analysis, and for comparison of distributions between

the signal-MC samples and the experimental data.

The luminosity function, which is a conversion factor between the e^+e^--based cross section σ_{ee} and the $\gamma^*\gamma$-based cross section $\sigma_{\gamma^*\gamma}$, is calculated in the same code. It is defined by

$$\frac{d^2\sigma_{ee}}{dQ^2dW} = 2\frac{d^2L_{\gamma^*\gamma}}{dQ^2dW}\sigma_{\gamma^*\gamma}(Q^2, W), \qquad (13)$$

where $2L_{\gamma^*\gamma}$ corresponds to the value of e^+e^--based integrated cross section per unit $\gamma^*\gamma$-based cross section in Eq. (2.16) of Ref. [19], and the differential luminosity function $d^2L_{\gamma^*\gamma}/dQ^2dW$ is calculated by performing a three-dimensional numerical integration over Q_2^2, ω_2, and $\Delta\varphi$. The factor of two incorporates for the contributions from the e-tag and p-tag processes included in the entire e^+e^--based cross section.

B. Event generation

The event generation is performed using the same integrand but including initial-state radiation (ISR) effects from the tag-side electron. Inclusion of ISR changes the kinematics and Q_1^2 significantly. Meanwhile, ISR from the untagged side has little effect because an ISR photon is nearly parallel not only to the initial-state electron but also to the final-state untagged electron. We use an exponentiation technique [22] for the photon emission based on the parameter $\eta = (2\alpha/\pi)(\log(Q_1^2/m_e^2) - 1)$ and the probability density for the photon energy distribution, $dP(r_k) \propto r_k^{\eta-1}dr_k$, where

$$r_k \equiv \frac{E^*_{\rm ISR}}{E^*_{\rm beam}}. \qquad (14)$$

As an approximation, the photon is always emitted along the incident electron direction on the tagged side. We limit the fractional energy of radiation to below $r_k^{\rm max} = 0.25$ in the MC generation.

In this configuration, the correction factor $1 + \delta$ to the tree-level cross section is close to unity [23]. Most of the events with large r_k, typically $r_k > 0.1$, are rejected by the selection criterion that uses $E_{\rm ratio}$ (the definition and criterion being described in Sec. IV A) by requiring energy-momentum conservation between the initial- and final-state particle systems without radiation. This effect is accounted for as a loss of efficiency for events with $r_k \leq r_k^{\rm max}$.

We generate events with a virtuality of the tagged-side photon Q_1^2 distributed with a constant form factor over its continuous range $Q^2 > 3.0$ GeV^2. The Q^2 value of each event is modified by ISR. We use the momentum of the ISR photon to determine the true Q^2 value in signal-MC events and to study the Q^2 dependence of the detection efficiency. We correct the experimental Q^2 dependence for the ISR effect using factors obtained from the signal MC (see Sec. VI D). We choose 15 different W points between 0.4 GeV and 2.5 GeV for the calculation of the luminosity function and event generation.

We use a GEANT3-based detector simulation [24] to study the propagation of the generated particles through the detector; the same code as for the experimental data is used for reconstruction and selection of the MC simulated events. We thus obtain the selection efficiency as functions of Q^2, W, and $|\cos\theta^*|$ for a flat φ^* dependence of the differential cross section. A correction for the observed φ^* dependence is discussed in Sec. VI C.

IV. EVENT SELECTION

In this section, we describe the event selection and present some raw distributions to compare with those from MC.

A. Selection criteria for signal candidate events

A signal event contains an energetic electron and four photons. The kinematical variables are calculated in the laboratory system unless otherwise noted; those in the e^+e^- or $\gamma^*\gamma$ c.m. frame are identified with an asterisk in this section. We require exactly one track that satisfies $p_t > 0.5$ GeV/c, $-0.8660 < \cos\theta < 0.9563$, $dr < 1$ cm, and $|dz| < 5$ cm. There must be no other tracks that satisfy $p_t > 0.1$ GeV/c, $dr < 5$ cm, and $|dz| < 5$ cm in the above angular range. Here, p_t is the transverse momentum in the laboratory frame with respect to the positron beam axis, θ is the polar angle of the momentum direction with respect to the z axis, and (dr, dz) are the cylindrical coordinates of the point of closest approach of the track to the beam axis. We also require one or more neutral clusters in the ECL, whose energy sum is greater than 0.5 GeV, as a pre-selection criterion for the experimental samples. These conditions are efficient in selecting a signal process within the kinematical regions of $e^+e^- \to e(e)\pi^0\pi^0$ in which one electron escapes detection at small forward angles.

For electron ID, we require $E/p > 0.8$ for the candidate electron track. The absolute value of the momentum of the electron must be greater than 1.0 GeV/c, where the electron energy is corrected for

photon radiation or bremsstrahlung in the following way. In a 3° cone around the track, we collect all photons in the range 0.1 GeV$< E_\gamma < p_e c/3$, where p_e is the measured absolute momentum of the electron track. The absolute momentum of the electron is replaced by $p_e + \Sigma E_\gamma$. The cosine of the polar angle for the electron (θ_e) must be within the range $-0.6235 < \cos\theta_e < 0.9481$, which is the sensitive region for the HiE and Clst4 triggers.

We search for a π^0 candidate reconstructed from a photon pair with each photon having an energy above 0.1 GeV and a polar angle in the range $-0.6235 < \cos\theta_\gamma < 0.9481$. We constrain the polar angle of the photons from at least one π^0 in the sensitive region of the ECL triggers by the latter condition, in order to reduce the systematic uncertainty of the trigger efficiency. The two-photon invariant mass is required to satisfy the criterion $0.115\ \mathrm{GeV}/c^2 < M_{\gamma\gamma} < 0.150\ \mathrm{GeV}/c^2$. This π^0 candidate is referred to as "$\pi1$".

In parallel, we search for π^0 candidates with the π^0-mass-constrained fit among all pairwise combinations of photons in the entire ECL region. We select only combinations of photon pairs whose goodness of fit satisfies $\chi^2 < 16$. If $\pi1$ is also selected by the mass-constrained fit, we replace the four-momentum of $\pi1$ by that of the result of the fit.

We require that only one more pion be found among the π^0 candidates from the mass-constrained fit which does not share any photons with $\pi1$. We refer to the second π^0 as "$\pi2$".

If there are two or more possible assignments of $\pi1$ and $\pi2$, we choose the one with the highest-energy photon to construct $\pi1$. If there are still two or more combinations that share the highest-energy photon in $\pi1$, we choose the one in which the other photon in $\pi1$ has the higher energy.

Figure 3 shows the $\gamma\gamma$ invariant-mass distribution when constructing $\pi1$ with a looser criterion of the two-photon invariant mass. The experimental data are compared with the distribution from the signal-MC sample using fits described below. The signal-MC distribution is fitted by the sum of a Crystal Ball function [25] and a linear function (signal component). Then, the experimental distribution is fitted by the sum of the signal component with the determined shape parameters and an additional linear function (background component), where the normalization and horizontal position for the signal component are allowed to float (resulting in a shift of the peak position by $-0.8\ \mathrm{MeV}/c^2$). The sole purpose of this fit is to compare the figures, which indicates a reasonable agreement and provides an estimate of the background contamination.

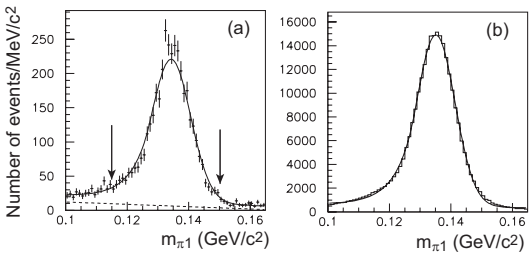

FIG. 3: (a) The experimental distributions for the $\gamma\gamma$ invariant mass forming $\pi1$. The arrows indicate the selection range. (b) The distribution from the signal MC for the same variable. Statistics of the MC figure are arbitrary. The fit for the comparison is shown by a solid curve in each of the distributions (see the text). The background component in the experimental data from the fit is shown by the dashed line.

We apply additional selection criteria for $\pi1$ and $\pi2$ to reduce contamination from low-energy background photons. The energy asymmetry for the two daughters ($\gamma1$ and $\gamma2$) of either pion, defined as

$$E_{\mathrm{asym}} = \frac{|E_{\gamma1} - E_{\gamma2}|}{E_{\gamma1} + E_{\gamma2}}, \tag{15}$$

must satisfy $E_{\mathrm{asym}} < 0.8$. We require that the π^0 energies and transverse momenta satisfy $E_{\pi1} > 0.4$ GeV, $E_{\pi2} > 0.3$ GeV, $E_{\pi1} + E_{\pi2} > 1$ GeV, $p_{t,\pi1} > 0.15\ \mathrm{GeV}/c$, and $p_{t,\pi2} > 0.15\ \mathrm{GeV}/c$, respectively. We require that the polar angle of $\pi2$ in the laboratory frame satisfy $-0.8660 < \cos\theta < 0.9563$.

We reject events with a back-to-back configuration of an electron and $\pi1$ in the e^+e^- c.m. frame, to suppress Bhabha events in which a track is not reconstructed; we require $\zeta^*(e,\pi1) < 177°$, where $\zeta^*(e,\pi1)$ is the opening angle between the electron and the $\pi1$ system.

We require the tagged lepton to have the correct charge sign ("right-sign") with respect to the beam from which it originates in the e^+e^- c.m. frame:

$$q_{\mathrm{tag}} \times (p^*_{z,e} + p^*_{z,\pi1} + p^*_{z,\pi2}) < 0, \tag{16}$$

where q_{tag} is the tagged lepton charge.

We apply a kinematical selection of $0.85 < E_{\mathrm{ratio}} < 1.1$, where E_{ratio} is defined as

$$E_{\mathrm{ratio}} = \frac{E^{*\mathrm{measured}}_{\pi^0\pi^0}}{E^{*\mathrm{expected}}_{\pi^0\pi^0}} \tag{17}$$

and $E^{*\mathrm{measured}}_{\pi^0\pi^0}$ ($E^{*\mathrm{expected}}_{\pi^0\pi^0}$) is the e^+e^- c.m. energy of the $\pi^0\pi^0$ system measured directly (expected by kinematics without radiation). This requirement

is motivated by a three-body kinematical calculation for $e^+e^- \to e(e)R$ that is to be followed by $R \to \pi^0\pi^0$, where R need not be a physical resonance because this is a kinematical calculation. We impose a four-momentum conservation condition $p_{\rm initial}(e^+e^-) = p_{\rm final}(e(e)R)$ wherein the direction of the R momentum is taken to be parallel to that of the observed $\pi^0\pi^0$ system in the e^+e^- c.m. frame. The expected energy of the $R(=\pi^0\pi^0)$ system, $E^{*\rm expected}_{\pi^0\pi^0}$, is obtained by assigning the measured $\pi^0\pi^0$ invariant mass to the R system.

In Fig. 4, we show a comparison of $E_{\rm ratio}$ between the data and signal MC, where we observe a sharp peak corresponding to the signal process in the data that is consistent with the MC. The distribution for "wrong-sign" events that have the opposite lepton charge to Eq. (16) is also shown; here, only a small peak is seen for the wrong-sign events near $E_{\rm ratio} = 1$. This means that the backgrounds from e^+e^- annihilation events, where the charge asymmetry of the tracks is not expected, are negligibly small. Meanwhile, there are significant right-sign backgrounds with a small $E_{\rm ratio}$. We discuss such events in Sec. V E.

We require transverse momentum balance in the e^+e^- c.m. frame, $|\Sigma \boldsymbol{p}^*_t| < 0.2$ GeV/c, where

$$|\Sigma \boldsymbol{p}^*_t| = |\boldsymbol{p}^*_{t,e} + \boldsymbol{p}^*_{t,\pi 1} + \boldsymbol{p}^*_{t,\pi 2}|. \qquad (18)$$

We show the distribution for $|\Sigma \boldsymbol{p}^*_t|$ (referred to as "p_t balance") in a wider range than the signal region in three different W ranges in Fig. 5, where the samples after the three-body kinematics condition by the $E_{\rm ratio}$ selection criterion applied are shown. The experimental distributions are compared with those of the signal-MC events. The signal peak near $|\Sigma \boldsymbol{p}^*_t| = 0$ is a little wider in the data than in the MC. This is partially due to the backgrounds in the data and partially due to non-inclusion of the finite-angle initial state radiation (ISR) on the tag side or the non-tag side. However, it is expected that the transverse momentum of the observed system, $|\Sigma \boldsymbol{p}^*_t|$, is dominated by those of the colliding virtual photons, which are taken into account in the MC simulation because the Q^2 of the electron after the ISR emission is expected to be smaller than Q^2 of the colliding photon emitted by the electron. This is supported by our previous study of the $|\Sigma \boldsymbol{p}^*_t|$ distribution for the $\gamma^*\gamma \to \pi^0$ process [10].

We find that events with $E_{\rm ratio} < 0.7$ do not peak at $|\Sigma \boldsymbol{p}^*_t| = 0$. These features show that some charged or neutral hadrons or photons from π^0 decay escape detection in these events. They are considered to come from multi-hadron production in two-photon processes or virtual pseudo-Compton scattering ($e^+e^- \to e(e)\gamma^*$, $\gamma^* \to$ hadrons) according to the observed asymmetry in the correct- and incorrect-charge sign events, with a leakage of these background components into the $E_{\rm ratio}$ signal region.

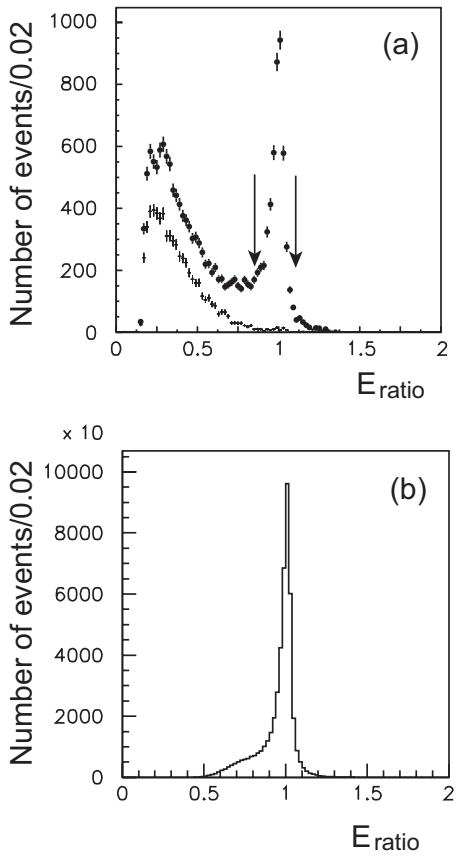

FIG. 4: The distributions for $E_{\rm ratio}$ for (a) the experimental data and (b) the signal-MC sample. The cross plots in (a) show the distribution for the wrong-sign events, and the arrows indicate the signal region. Statistics of the MC figure are arbitrary.

The $E_{\rm ratio}$ and $|\Sigma \boldsymbol{p}^*_t|$ distributions are discussed in more detail for background estimation, in Sec. V.

B. Assignment of kinematical variables for a signal event

We assign four kinematical variables Q^2, W, $|\cos\theta^*|$, and φ^* to each signal candidate event. The angles $|\cos\theta^*|$ and φ^* are defined in the $\gamma^*\gamma$ c.m. frame, where the direction of γ^* has $\cos\theta^* = 1$ and the azimuthal direction of the recoiling electron defines $\varphi^* = 0$ (Fig. 2). Note that only these two variables are defined in the $\gamma^*\gamma$ c.m. frame. In contrast, all the other variables with an asterisk appearing be-

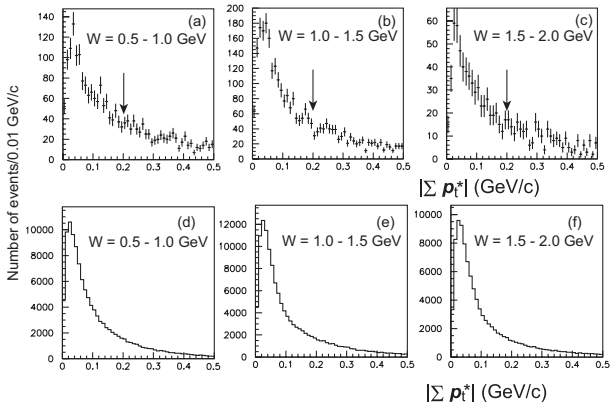

FIG. 5: (a,b,c) The distributions for the p_t balance for the data samples in three different W ranges indicated in each panel. The arrows show the selection region. (d,e,f) The corresponding distributions from the signal MC. Statistics of the MC figures are arbitrary.

low are defined in the e^+e^- c.m. frame.

The negative of the invariant mass squared, Q^2, of the virtual incident photon is calculated using the measured four-momentum of the detected electron (p_e) from

$$\begin{aligned} Q^2_{\rm rec} &= -(p_{\rm beam} - p_e)^2 \\ &= 2E^*_{\rm beam}E^*_e(1 + q_{\rm tag}\cos\theta^*_e), \end{aligned} \qquad (19)$$

where $p_{\rm beam}$ is the nominal four-momentum of the beam particle with the same charge as the detected electron; the right-hand side is given by the beam energy $E^*_{\rm beam}$ and the observables of the tagged electron in the e^+e^- c.m. frame. We do not apply a correction for initial-state radiation (ISR) on an event-by-event basis; instead, this effect is taken into account in the correction for the differential cross section, as mentioned in Sec. VI.

The c.m. energy of the incident $\gamma^*\gamma$ collision, W, is the invariant mass of the final-state $\pi^0\pi^0$ system. The pion scattering angle θ^* is defined in the $\gamma^*\gamma$ c.m. frame as an angle between the virtual photon and that of one of the produced pions. In case an ISR photon is emitted in the tagged-electron side, the direction of the virtual photon is slightly misreconstructed and induces an error in $\cos\theta^*$. However, the change due to this effect is typically ± 0.01 in $\cos\theta^*$. This is smaller than the angular resolution, typically $\sigma_{\cos\theta^*} = 0.02$, and the bin width, 0.2, and thus we neglect the effect.

There is a two-fold symmetry for the two sides of the plane, since $\frac{d\sigma}{d\varphi^*}(\varphi^*) \equiv \frac{d\sigma}{d\varphi^*}(2\pi - \varphi^*)$, so this angle is limited to the range $0 \le \varphi^* \le \pi$.

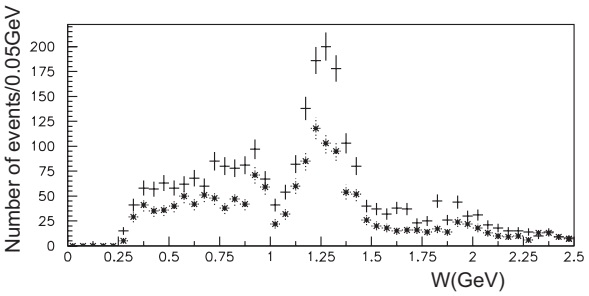

FIG. 6: The experimental distributions for W of the signal candidates for 3 GeV^2 (5 GeV^2) $< Q^2 <$ 30 GeV^2 for the e-tag (p-tag) samples. Backgrounds are not subtracted. The cross and asterisk plots are for the e-tag and p-tag samples, respectively.

C. Comparison of the experimental candidates with the signal-MC events

In this subsection, we show various distributions of the selected signal candidates. Backgrounds are not subtracted in the experimental data. Data distributions are compared with the signal MC, where a uniform angular distribution and a representative Q^2 dependence are assumed. As most Q^2 and angular dependence in these figures arise from kinematics, such comparisons are meaningful, but no perfect agreement between data and MC should be expected.

The experimental W distribution is shown in Fig. 6 for $W \le 2.5$ GeV. For comparison, the corresponding distributions from the signal MC are also shown in the following figures. In Figs. 7 – 9, all events within $Q^2_L < Q^2 <$ 30 GeV^2 and 0.5 GeV $< W <$ 2.1 GeV are integrated, where $Q^2_L = 3$ GeV^2 ($= 5$ GeV^2) for the e-tag (p-tag) sample. We do not use the data below $W < 0.5$ GeV because the signal efficiency and the signal-to-background ratio decrease steeply below that energy. No large discrepancy between the data and signal MC is seen in all the figures. This implies that the MC is a faithful representation of reality and the backgrounds in the experimental data are not very large. The difference in the pion energy distributions reflects the difference in its angular distribution in the $\gamma^*\gamma$ c.m. frame between the data and signal MC, with the uniform angular distribution for the latter.

V. BACKGROUND ESTIMATION

We consider several sources of possible background processes that could be misidentified as the signal

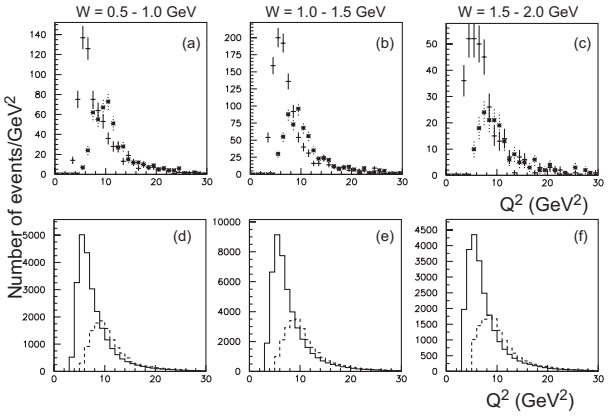

FIG. 7: (a,b,c) The Q^2 distributions for the data samples in three different W ranges indicated above each panel. The cross and asterisk plots are for the e-tag and p-tag samples, respectively. (d,e,f) The corresponding distributions from the signal MC, where the solid and dashed histograms are for the e-tag and p-tag samples, respectively. Statistics of the MC figures are arbitrary, but the scale is common for the e- and p-tags so their ratio could be compared between MC and data.

process.

A. Single pion production process

Backgrounds from the single pion production, $e^+e^- \to e(e)\pi^0$, with one fake π^0 that is wrongly reconstructed, are estimated by MC simulation of the process. From our previous measurement [10], we know the cross section of this process with a sufficient accuracy for this purpose. From the MC study, the contamination is estimated to be less than one event in the whole sample of candidate events (about 3700 events) and is enhanced in the forward angular region in the c.m. frame, as shown in Fig. 10(c). As the estimated number of events is small, we neglect this background source. The Q^2 dependence of this background source is expected to be similar to that of the signal process.

B. Radiative Bhabha process

The radiative Bhabha process with the virtual Compton scattering topology, $e^+e^- \to e(e)\gamma$, which has a relatively large cross section, has been proved to give only a small contribution to the present measurement. This is verified in the $\pi1$ and $\pi2$ mass distributions (Fig. 8), where the pion peaks in the

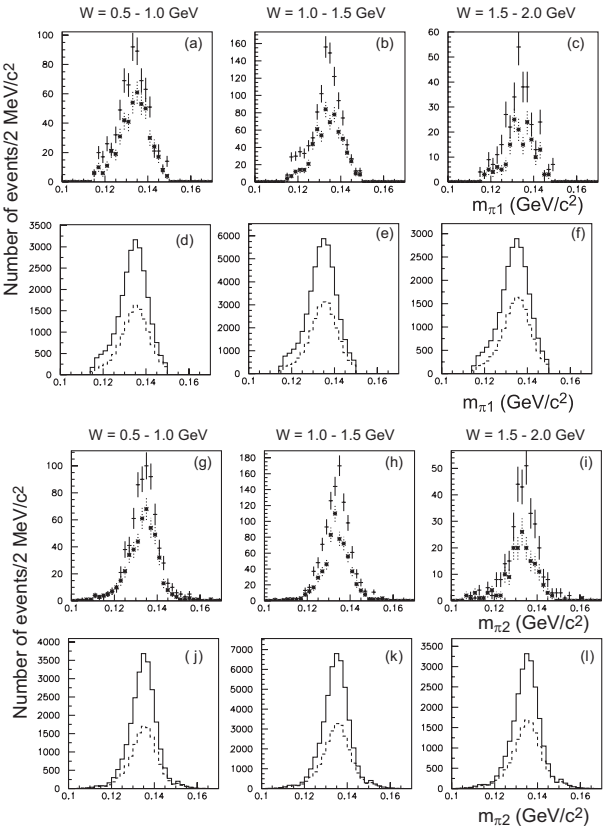

FIG. 8: (a,b,c,g,h,i) The distributions for the $\gamma\gamma$ invariant mass to construct $\pi1$ (a,b,c) and $\pi2$ (g,h,i) for the data samples in three different W ranges indicated above each panel. (d,e,f,j,k,l) The corresponding distributions from the signal MC for $\pi1$ (d,e,f) and $\pi2$ (j,k,l). The legend and comments are the same as those in Fig. 7.

experimental data with a high purity compared to the signal-MC samples. This background must be less than 5% according to the shape of the $m_{\pi1,2}$ distribution. However, we must note that this background forms a broad enhancement near the pion mass when the high-energy photon is converted to an e^+e^- pair in front of the ECL. The measured Q^2 values for the virtual Compton scattering tend to populate the region of higher values than in the signal process, and the background should be relatively large in the high-Q^2 region.

The estimation of the contamination from this background process using a background-MC sample is very difficult because of the large MC statistics needed due to the large cross section of the process and the significant suppression in the event selection. Thus, we estimate the contamination using distributions of the experimental signal candidates.

In presence of both of the described background

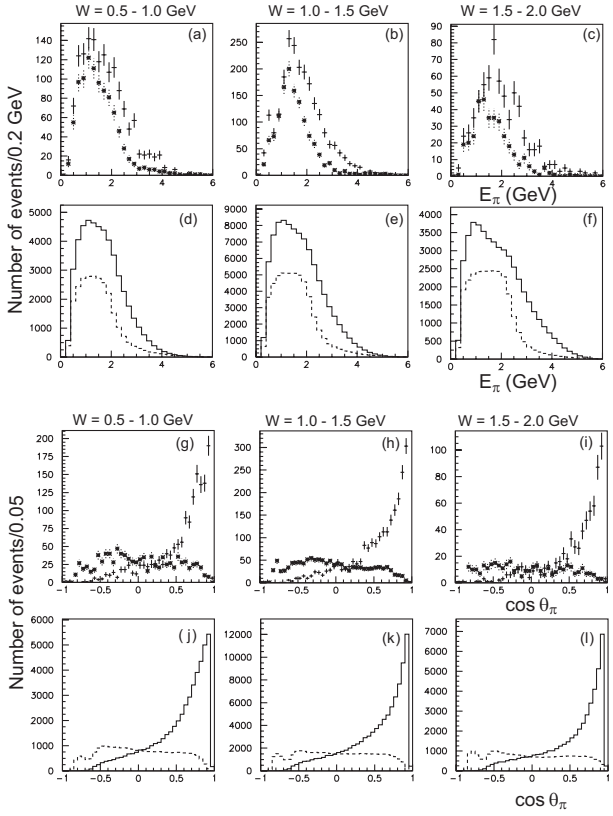

FIG. 9: (a,b,c) The distributions for the laboratory energy of $\pi 1$ and $\pi 2$ for the data samples in three different W ranges indicated above each panel. (d,e,f) The corresponding distributions from the signal MC. (g,h,i) and (j,k,l) are the distributions for the laboratory angle of $\pi 1$ and $\pi 2$ for the data samples in the indicated W ranges for the experimental samples and MC samples, respectively. The legend and comments are the same as those in Fig. 7.

processes, single pion production and the radiative Bhabha process, at least one of the two π^0s reconstructed is not a true π^0. A fake π^0 is wrongly reconstructed from the beam background or electronic noise. If such a background π^0 had large reconstructed energy, the event would have been rejected by the p_t-balance selection criterion. Therefore, these fake pions remain in the signal event sample only if the noise has small reconstructed energy. In addition, such noise photons populate the lowest energy region just above the energy thresholds for a photon or a neutral pion for the selection. Consequently, the c.m. scattering angle in the two-photon system tends to be reconstructed in the forward regions because of the unbalanced laboratory energies between the two pions and the Lorentz boost of the two-pion system along the beam axis, just as expected in the single-π^0 production case. However, as seen in Fig. 10(a), no visible enhancement is seen even in the most forward region $|\cos\theta^*| > 0.9$, where the number of the signal events is small according to the small signal acceptance (Fig. 10(b)) in the angular distribution for the entire experimental signal candidates. Figure 11(a) shows the $\pi 1$ and $\pi 2$ mass distribution for the events with $|\cos\theta^*| > 0.9$ in comparison with the signal-MC expectation and the experimental data for $|\cos\theta^*| < 0.9$ (Fig. 11(b) and (c), respectively). It is difficult to estimate the non-π^0 backgrounds quantitatively from these figures.

In our previous study [10], we found that the backgrounds from virtual Compton scattering have a high-energy neutral pion from misreconstruction of an e^+e^- conversion of the single photon, which simulates two photons with a high probability. Its characteristic feature is a small polar angle difference $\Delta\theta$ due to the effect of the magnetic field. It is found experimentally that the backgrounds concentrate strongly at $\Delta\theta\, E_{\gamma\gamma} < 0.05$ rad·GeV [10]. Figure 12 shows the distribution of $\Delta\theta\, E_{\gamma\gamma}$ for $\pi 1$. We estimate the yield of the backgrounds from the virtual Compton process to be around 10 events, which are seen as an enhancement in the region $\Delta\theta\, E_{\gamma\gamma} < 0.05$ rad·GeV, out of the 67-event subsample with $|\cos\theta^*| > 0.9$ and 0.5 GeV$< W <$ 2.1 GeV. We thus estimate that the background fraction is about 15% for $|\cos\theta^*| > 0.9$, although its uncertainty is large. We do not find any sign of background from this source in the region $|\cos\theta^*| < 0.9$.

C. $\pi^0\gamma$ production process

Backgrounds from the $\pi^0\gamma$ production, $e^+e^- \to e(e)\pi^0\gamma$, are dominated by the virtual pseudo-Compton scattering process of ω-meson production, $e^+e^- \to e(e)\omega$. We know the cross section of this process with sufficient accuracy from our previous measurement [10] to estimate this contamination from the background-MC study, as described below.

The W, Q^2, and $|\cos\theta^*|$ dependences are based on the MC. Figure 13 shows the distributions of the background from the process $e^+e^- \to e(e)\omega$, $\omega \to \pi^0\gamma$ in the Q^2-W, and $|\cos\theta^*|$-W directions. This background is enhanced in the W region near the ω mass ($W = 0.7$ – 0.9 GeV) in the high-Q^2 region ($Q^2 > 12$ GeV^2). The total number of events contaminating the signal process is estimated to be about 9 events, of which only 6 events for $Q^2 > 12$ GeV^2 are expected to have a non-negligible effect compared to the signal yield. The $|\cos\theta^*|$ dis-

tribution is approximately flat so the behavior of this background is very different from the former background sources where both photons constituting one pion originated from noise. We find no visible enhancement in the 0.7 – 0.9 GeV region in the observed W distribution, as expected from the small contamination of the background process.

D. Three-π^0 production process

The three-pion production process, $\gamma^*\gamma \to \pi^0\pi^0\pi^0$, is wrongly selected as the signal candidate if one non-energetic pion escapes detection. As three-pion production in single-tag two-photon collisions has not been measured to date, we estimate the contamination by referring to the corresponding zero-tag measurement.

The $\pi^+\pi^-\pi^0$ production in the zero-tag process has been measured by the L3 collaboration [26] and shows that the process is dominated by the $a_2(1320)$ and a structure near 1.7 GeV ($a_2(1700)$ and potential $\pi_2(1670)$ production decaying to $\rho^0\pi^0$ or $f_2(1270)\pi^0$). However, the three-neutral-pion production is strongly suppressed because ρ^0 does not decay to $\pi^0\pi^0$ and $a_2(1700) \to f_2(1270)\pi^0$ has not been observed definitively. The L3 measurement only provides an upper limit for $\pi_2(1670)$ production from the two-photon process. A measurement of a finite value for $\gamma\gamma \to \pi_2(1670) \to \pi^0\pi^0\pi^0$ production is reported by the Crystal Ball experiment [27] but it is not consistent with the L3 upper limit.

We estimate that $\pi^0\pi^0\pi^0$ production is about 4% of $\pi^0\pi^0$ production in the zero-tag two-photon process [28, 29] in the e^+e^--based cross section, according to the measurement of L3 for $\gamma\gamma \to a_2(1700) \to f_2(1270)\pi^0$ [26]. We confirm this estimate by our count of zero-tag $\gamma\gamma \to \pi^0\pi^0\pi^0$ candidate events, requiring three neutral pions in an event, from the Belle data samples. Our estimate of the cross section is somewhat smaller than that from the above Crystal Ball measurement [27], but is consistent with it within about a factor of two.

We assume that the cross section ratio of the two processes, $\pi^0\pi^0\pi^0$ to $\pi^0\pi^0$, is the same between the zero-tag and single-tag processes. Taking into account the selection efficiency for the background events and the background subtraction using the p_t-balance distribution (applied in Sec. VI B), the estimated contamination is less than 0.5% of the signal yield, where the $\pi^0\pi^0\pi^0$ background does not peak near $|\Sigma \boldsymbol{p}_t^*| = 0$, like for the other non-exclusive processes described in the following section.

The contribution from the process $\gamma^*\gamma \to \eta' \to \pi^0\pi^0\pi^0$ is separately estimated using the η'-TFF [11], the branching fraction, and generated background-MC samples for the process. We find that the expected contribution for $W > 0.5$ GeV is about 0.3 events. Thus, we conclude that the contribution of this background is negligibly small.

E. Other non-exclusive processes

The other non-exclusive background processes, $e^+e^- \to e(e)\pi^0\pi^0X$, where X denotes multiple hadrons, are in general subdivided into two-photon (C-even) and virtual pseudo-Compton (bremsstrahlung, C-odd) processes, but they interfere with each other if the same X is allowed for both processes. The majority of such background events populate the small $E_{\rm ratio}$ region, *e.g.*, less than 0.7. This feature is distinct from the aforementioned background processes that can populate the region near $E_{\rm ratio} = 1$. These backgrounds also do not peak near $|\Sigma \boldsymbol{p}_t^*| = 0$.

From Fig. 4, we expect that the low-$E_{\rm ratio}$ component could leak into the signal region. We estimate the relative ratio of the non-exclusive backgrounds to the signal yield by counting the number of events in the subregion of the signal region ($0.85 < E_{\rm ratio} < 0.925 \cap 0.1$ GeV/c $< |\Sigma \boldsymbol{p}_t^*| <$ 0.2 GeV/c) where the background component would be relatively large. We assume that the backgrounds are distributed as a linear function in $0 < |\Sigma \boldsymbol{p}_t^*| <$ 0.2 GeV/c and in $0.85 < E_{\rm ratio} < 1$, vanishing at $|\Sigma \boldsymbol{p}_t^*| = 0$ and $E_{\rm ratio} = 1$, respectively, factorized for the two directions. The fraction of the backgrounds falling in the above subregion is calculated to be 9/16 of that in the entire signal region, according to the distribution. We also estimate the fraction of signal events coming into the same region using the signal-MC sample. We thus determine the expected number of the background events from this information.

In addition, we use the W and Q^2 dependence of the $E_{\rm ratio}$ sideband events, which are extracted from the experimental data in $0.7 < E_{\rm ratio} < 0.8$ as ancillary information for the kinematical regions with low statistics. The normalization of the background is determined in the first method in a high-statistics region; we extrapolate it to different W and Q^2 regions with lower statistics assuming the dependence observed in the $E_{\rm ratio}$ sideband region.

We show the $E_{\rm ratio}$ and $|\Sigma \boldsymbol{p}_t^*|$ distributions in the signal region of the experimental and signal-MC samples in Figs. 14 and 15, respectively. The dashed lines in the panels for the experimental data show the estimated non-exclusive background.

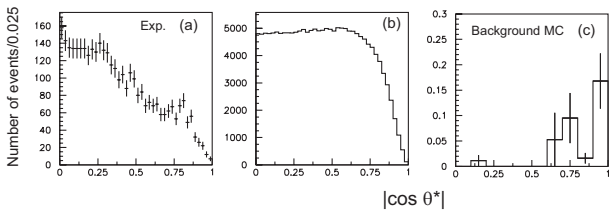

FIG. 10: The $|\cos\theta^*|$ distributions for (a) the experimental signal candidates, (b) the signal MC with the isotropic generation for $|\cos\theta^*|$, and (c) the background-MC events for the single-pion production process, where the yield is scaled to the expected contamination in the set of all signal candidates. The error bars are statistical from the MC samples but are not proportional to square root of the number of events because each event in the MC sample has a variable weight to reproduce the experimental Q^2 dependence. For (b), the normalization is arbitrary.

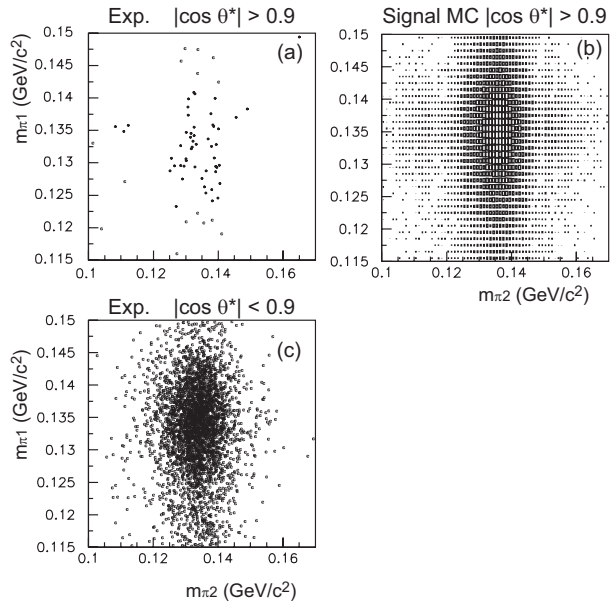

FIG. 11: Scatter plot for the $\gamma\gamma$ invariant masses for $\pi1$ and $\pi2$ for (a) the experimental signal candidates for $|\cos\theta^*| > 0.9$, (b) the signal-MC samples for $|\cos\theta^*| > 0.9$, and (c) the experimental signal candidates for $|\cos\theta^*| < 0.9$.

The details of the background subtraction are described in Sec. VI B.

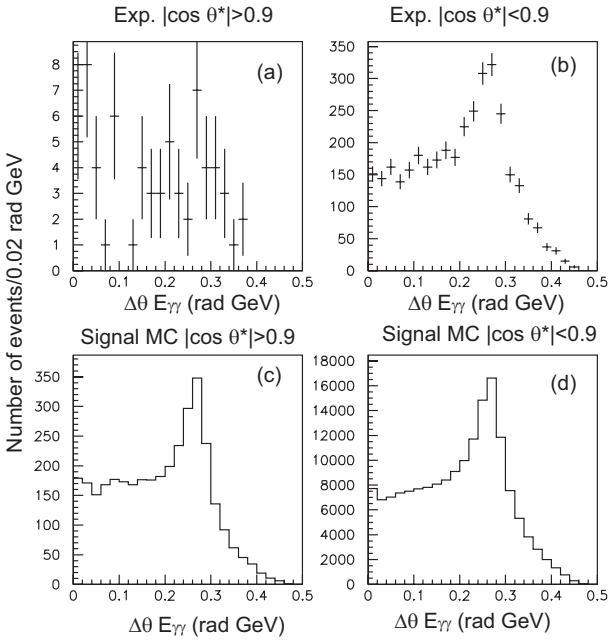

FIG. 12: The distributions of $\Delta\theta E_{\gamma\gamma}$ for (a) the experimental signal candidates in $|\cos\theta^*| > 0.9$ and (b) in $|\cos\theta^*| < 0.9$. Similar plots for (c) the signal-MC samples in $|\cos\theta^*| > 0.9$ and (d) $|\cos\theta^*| < 0.9$. The statistics of the MC figures are arbitrary.

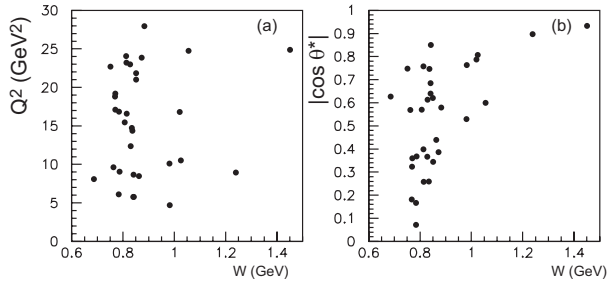

FIG. 13: The distribution of background events estimated from the MC for the process $e^+e^- \to e(e)\omega$, $\omega \to \pi^0\gamma$ in the Q^2 versus W and $|\cos\theta^*|$ versus W scatter plots. About three events in each plot correspond to a contamination of one event in the present signal-candidate sample.

VI. DERIVATION OF THE DIFFERENTIAL CROSS SECTION

We first define and evaluate the e^+e^--incident-based cross section separately for the p-tag and e-tag samples. Then we derive the differential cross section of the process $\gamma^*\gamma \to \pi^0\pi^0$.

The e^+e^--incident-based differential cross section

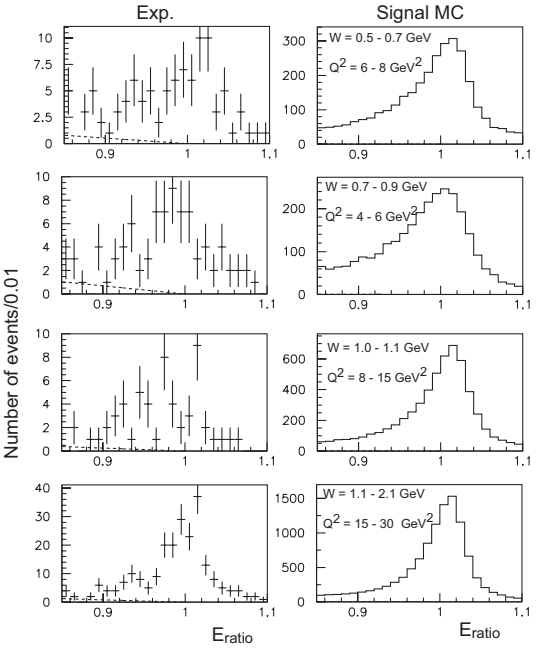

FIG. 14: Comparison between the experimental (left) and signal-MC (right) distributions for $E_{\rm ratio}$ of events in the signal regions. Each row corresponds to the same W and Q^2 regions indicated in the right panel. The dashed lines show the estimated non-exclusive background, which is assumed to distribute linearly with the horizontal variable. Statistics of the MC figures are arbitrary.

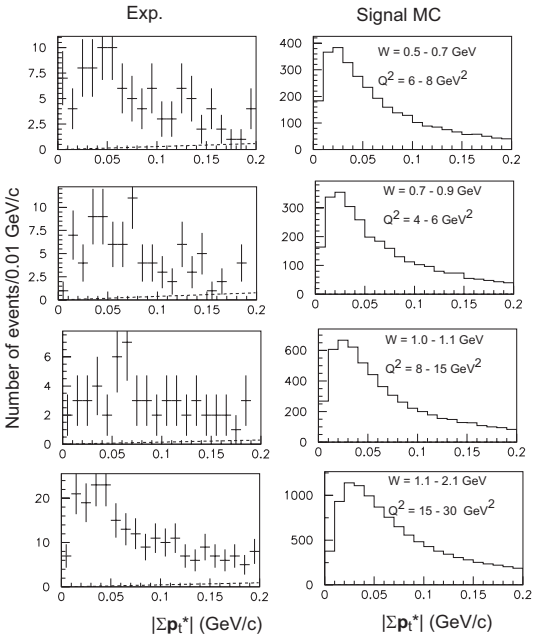

FIG. 15: Comparison between the experimental (left) and signal-MC (right) distributions for the p_t balance of events in the signal regions. Each row corresponds to the same W and Q^2 regions indicated in the right panel. The dashed lines show the estimated non-exclusive background, which is assumed to distribute linearly with the horizontal variable. Statistics of the MC figures are arbitrary.

is written as

$$\left(\frac{d^3\sigma_{ee}}{dW\,d|\cos\theta^*|\,dQ^2}\right)_{x-\rm tag} = \frac{Y_{x-\rm tag}(W,|\cos\theta^*|,Q^2)}{\varepsilon'_{x-\rm tag}(W,|\cos\theta^*|,Q^2)\Delta W\Delta|\cos\theta^*|\Delta Q^2\int\mathcal{L}dt\mathcal{B}^2}, \quad (20)$$

where the yield Y and the uncorrected efficiency obtained by the signal MC ε' are separately evaluated for p-tag and e-tag, for a consistency check. The measurement ranges of W, $|\cos\theta^*|$, and Q^2 and the corresponding bin widths ΔW, $\Delta|\cos\theta^*|$, and ΔQ^2 are summarized in Table III, where the differential cross section was first calculated with $\Delta W = 0.05$ GeV and $\Delta|\cos\theta^*| = 0.1$, and then two adjacent W and $|\cos\theta^*|$ bins are combined (for W only above $W > 1.1$ GeV) with an arithmetic mean. Here, $\int\mathcal{L}dt$ is the integrated luminosity of 759 fb^{-1} and $\mathcal{B}^2 = 0.9766$ is the square of the decay branching fraction $\mathcal{B}(\pi^0 \to \gamma\gamma)$.

We take into account the difference of the beam energies in evaluating ε'. Since the efficiency and the luminosity function depend on the beam energy, we construct the corrected efficiency using the ratio of the products of the efficiency, luminosity function, and the integrated luminosity for two cases: that the products are combined for the different beam energies in the experiment and that all the experiment would be done at the sole $\Upsilon(4S)$ energy with the same total integrated luminosity as in the experiment. Thus, the e^+e^--based cross section measured for the energy of $\Upsilon(4S)$, 10.58 GeV, is obtained.

After confirming the consistency between the p- and e-tag measurements to ensure validity of the efficiency corrections (described in Sec. VI A), we combine their yields and efficiencies using the formula which builds in the equality of the efficiency-corrected yields for both measurements,

$$\frac{d^3\sigma_{ee}}{dW\,d|\cos\theta^*|\,dQ^2} = \frac{Y(W,|\cos\theta^*|,Q^2)(1-b(W,|\cos\theta^*|,Q^2))}{\varepsilon'(W,|\cos\theta^*|,Q^2)\Delta W\Delta|\cos\theta^*|\Delta Q^2\int\mathcal{L}dt}, \quad (21)$$

where $Y = Y_{\rm p-tag} + Y_{\rm e-tag}$, $\varepsilon' = (\varepsilon'_{\rm p-tag} + \varepsilon'_{\rm e-tag})/2$, and b is the background fraction combined for p- and e-tags, which is subtracted here. For the region $Q^2 =$ 3 – 5 GeV^2, we do not use the p-tag data because its

TABLE III: The measurement range and bin widths for three-dimensional variables $(W, |\cos\theta^*|, Q^2)$.

Variable	Measurement range	Bin width	Unit	Number of bins
W	0.5 – 1.1	0.05	GeV	12
	1.1 – 2.1	0.1		10
$\lvert\cos\theta^*\rvert$	0.0 – 1.0	0.2		5
Q^2	3.0 – 5.0 (e-tag only)	1.0	GeV^2	2
	5.0 – 6.0	1.0		1
	6.0 – 12.0	2.0		3
	12.0 – 15.0	3.0		1
	15.0 – 20.0	5.0		1
	20.0 – 30.0	10.0		1

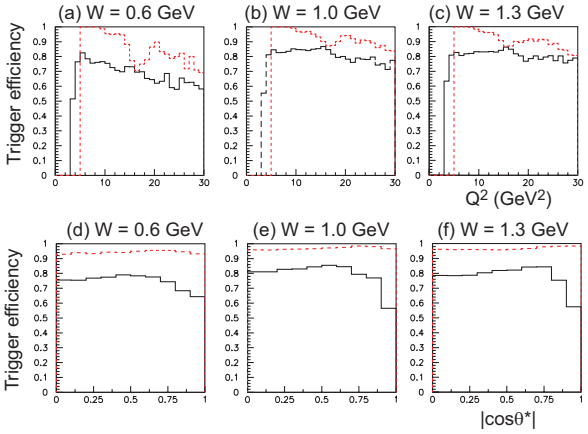

FIG. 16: Trigger efficiency estimated by the signal-MC samples and trigger simulator. The solid (black) and dashed (red) histograms are for e-tag and p-tag events, respectively. The results are for the three W points indicated above each panel: (a,b,c) the Q^2 dependence for the isotropically generated π^0 pairs in the $\gamma^*\gamma$ c.m. system; (d,e,f) the scattering- (polar-) angle dependence of π^0 in the $\gamma^*\gamma$ c.m. system. The Q^2 range 3 GeV^2 (5 GeV^2) $< Q^2 <$ 30 GeV^2 is integrated for the e-tag (p-tag) plot.

statistical accuracy is much worse than for the e-tag sample. There, as a result, the cross-section value in the e-tag measurement is simply doubled.

Finally, the e^+e^--incident-based differential cross section is converted to that based on $\gamma^*\gamma$-incident by dividing by the single-tag two-photon luminosity function $d^2L_{\gamma^*\gamma}/dW dQ^2$, which is a function of W and Q^2. We use the relation

$$\frac{d\sigma_{\gamma^*\gamma}}{d|\cos\theta^*|} = \frac{d^3\sigma_{ee}}{dW d|\cos\theta^*| dQ^2} \frac{f}{2\frac{d^2L_{\gamma^*\gamma}}{dW dQ^2}(1+\delta)(\varepsilon/\varepsilon')\varepsilon'}. \quad (22)$$

The factors δ, ε, and f correspond to the radiative correction, efficiency corrected for the φ^* dependence of the differential cross section, and the unfolding effect that accounts for migrations between the different Q^2 bins, respectively, which are explained in more detail in the subsections below.

A. Efficiency plots and consistency check of the p-tag and e-tag measurements

Figure 16 shows the trigger efficiencies obtained from the signal-MC samples and trigger simulator. The trigger efficiency is defined for events within the selection criteria. The W dependence of the trigger efficiency is mild in the measurement region. The dip-bump structure seen in the Q^2 dependence for the p-tag efficiency is an artifact of the Bhabha-veto logic in the HiE trigger.

Figure 17 shows the efficiencies in which all the selection and trigger conditions are taken into account. They are provided as a function of W and $|\cos\theta^*|$ for the selected Q^2 bins of the p- or e-tag samples. These efficiencies are obtained from the signal-MC events, which are generated assuming an isotropic angular distribution of the pions in the $\gamma^*\gamma$ c.m. frame. Efficiency corrections for the φ^* dependence are not taken into account in these figures.

Our accelerator and detector systems are asymmetric between the positron and electron incident directions and energies, and separate measurements of the p-tag and e-tag samples provide a good validation check for various systematic effects of the trigger, detector acceptance, and selection conditions. Figures 18 and 19 compare the e^+e^--based cross section measured separately for the p- and e-tags. They are expected to show the same cross section according to the C symmetry if there is no systematic bias. The results from the two tag conditions are consistent within statistical errors.

B. Background subtraction

We have estimated the background yields in the signal samples using the background-process-MC samples for the single pion production, $e^+e^- \to e(e)\pi^0$, and the $\pi^0\gamma$ production dominated by $e^+e^- \to e(e)\omega$, $\omega \to \pi^0\gamma$. These are described in Ref. [10], where their yields are normalized based on the observations.

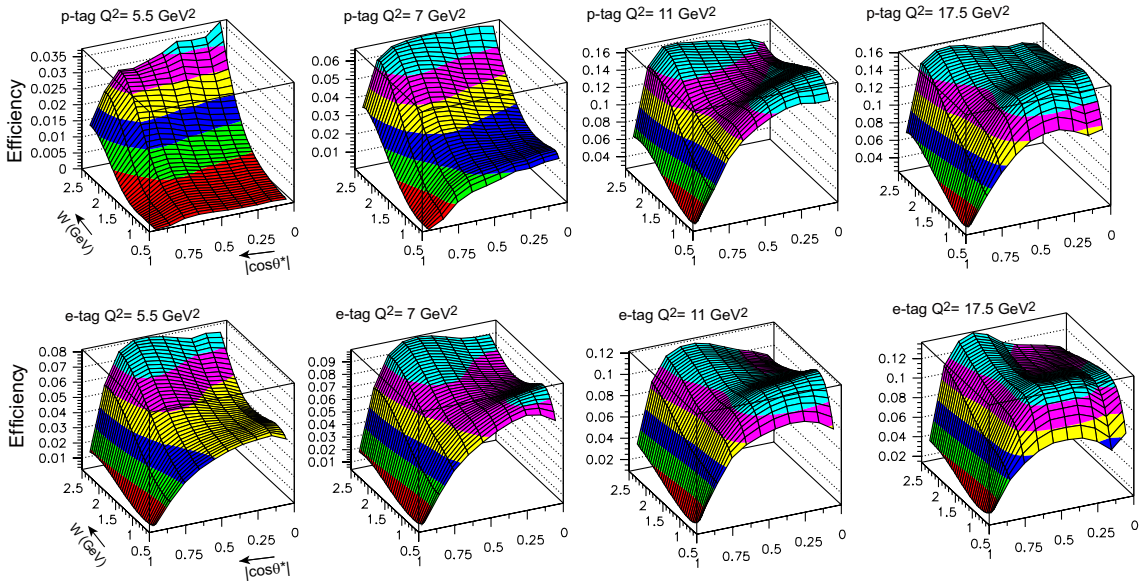

FIG. 17: Efficiency estimated from the signal-MC samples passed through all the selection and trigger conditions. Each panel provides the W and $|\cos\theta^*|$ dependences of the efficiency for the four selected Q^2 bins for each of the p- or e-tags. The contour levels shown by different colors are not common across the panels.

As mentioned in Sec. V, the estimated total yields for the sum of p- and e-tags are less than one and nine events for the single pion and the $\pi^0\gamma$ production backgrounds, respectively.

The single-pion background is small, and we do not subtract its contribution but rather include its effect in the systematic uncertainty due to subtraction of the virtual Compton scattering.

For the $\pi^0\gamma$ production, the background is estimated to be 2%, 6%, and 13% of the signal candidate yields for the Q^2 bins of 12 – 15 GeV^2, 15 – 20 GeV^2, and 20 – 30 GeV^2, respectively, independently of W and $|\cos\theta^*|$, and is subtracted. For the bins at $Q^2 \leq 12$ GeV^2, we neglect this background source.

The details of the estimation of the background contributions from the virtual Compton process are discussed in Sec. V B. We estimate that the signal-candidate yield in each $|\cos\theta^*| > 0.9$ bin contains (15 ± 15)% of the background from this process, and we derive the differential cross section for the $|\cos\theta^*| > 0.8$ bin. We estimate systematic uncertainties conservatively because possible Q^2 dependence and the background from the single-pion production process with similar properties are neglected here, and the contamination could be sensitive to the noise conditions. The error size is estimated from $\Delta\theta\, E_{\gamma\gamma}$ and $|\cos\theta^*|$ distributions for several different conditions. The uncertainties of the background estimation for different kinematical regions are discussed in Sec. VI F.

We neglect the contribution of the $\pi^0\pi^0\pi^0$ production process because it is estimated to be less than 1% of the signal process (Sec. V D).

The contamination of the other non-exclusive background processes is estimated using the $E_{\rm ratio}$ and $|\Sigma \boldsymbol{p}_t^*|$ variables as described in Sec. V E. We estimate the fraction of the background in each of the (W, Q^2) regions to be between 3% and 12%. This background fraction has no prominent $|\cos\theta^*|$ dependence and we neglect it.

In subtraction of the background yields, we multiply the observed yield by the expected ratio of the background to the observed yields in each bin, as represented by the $(1-b)$ factor in Eq. (21).

C. Efficiency corrections

The efficiency after the integration over φ^* is calculated using the signal MC, assuming a flat φ^* distribution. We correct the efficiency according to the actual non-uniformity in φ^* observed in the data. This correction is necessary in case both the efficiency (ε) and the differential cross section ($d\sigma/d\varphi^*$) have a φ^* dependence.

We partition the kinematical region of the measurement into three-dimensional (W, $|\cos\theta^*|$, Q^2)

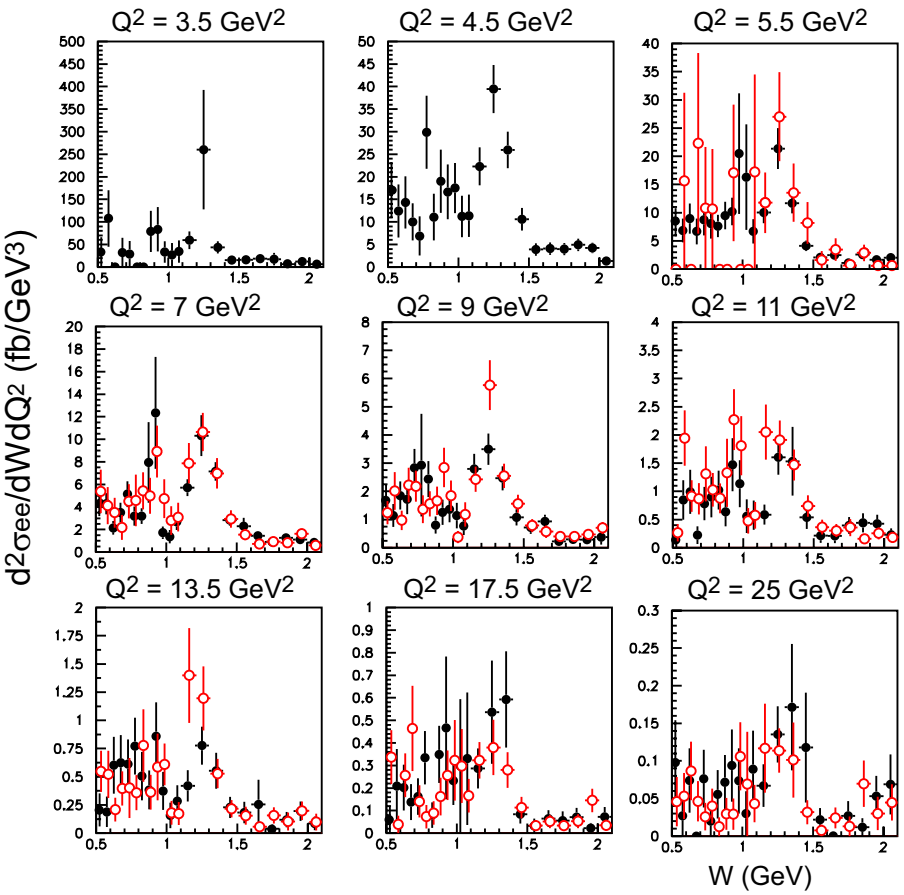

FIG. 18: The W dependence of the e^+e^--based cross section in each Q^2 bin. The full $|\cos\theta^*|$ range (0 to 1) is integrated. The closed circles (open circles) are for the e-tag (p-tag) measurements. The plotting location for each p-tag point is shifted slightly to improve the visibility of error bars. The efficiency corrections and background subtraction are applied.

rectangular-prism cells defined by 0.5 GeV $< W <$ 1.1 GeV, 1.1 GeV $< W <$ 1.6 GeV, and 1.6 GeV $< W <$ 2.1 GeV; five equal-width bins in $|\cos\theta^*|$; 3 GeV^2 $< Q^2 <$ 8 GeV^2, 8 GeV^2 $< Q^2 <$ 12 GeV^2, and 12 GeV^2 $< Q^2 <$ 30 GeV^2.

Due to limited statistics, we take such a coarse binning for the W and Q^2 directions, taking into account qualitative changes of $|\cos\theta^*|$ dependence of the differential cross section. We estimate the efficiency correction factor, ε/ε', in each of the cells.

The signal-MC distribution after the selection behaves as $N_{\rm MC}(\varphi^*) \propto \varepsilon(\varphi^*)$ and the experimental distribution as $N_{\rm EXP}(\varphi^*) \propto \varepsilon(\varphi^*)P(\varphi^*)$, where $P(\varphi^*) \propto d\sigma/d\varphi^*$. Then, the efficiency correction factor is calculated as

$$\frac{\varepsilon}{\varepsilon'} = \frac{\pi \int_0^\pi \varepsilon(\varphi^*)P(\varphi^*)d\varphi^*}{\int_0^\pi \varepsilon(\varphi^*)d\varphi^* \int_0^\pi P(\varphi^*)d\varphi^*}. \quad (23)$$

The φ^* dependence of the efficiency and the φ^*-differentiated cross section are obtained by $\varepsilon(\varphi^*) \propto N_{\rm MC}(\varphi^*)$ and $P(\varphi^*) \propto N_{\rm EXP}(\varphi^*)/N_{\rm MC}(\varphi^*)$, respectively. We then expand each function as a Fourier series,

$$N_{\rm MC}(\varphi^*) = A(1 + c\cos\varphi^* + d\cos 2\varphi^* + ...) \quad (24)$$

and

$$N_{\rm EXP}(\varphi^*)/N_{\rm MC}(\varphi^*) = B(1 + a\cos\varphi^* + b\cos 2\varphi^*), \quad (25)$$

where the coefficients are determined by fitting. There are no sine terms because we expect symmetry between φ^* and $-\varphi^*$ for these functions, or we can regard them as the sum of the functions in the positive and negative φ^* regions, $g(\varphi^*) = f(\varphi^*)+f(-\varphi^*)$ $(0 \le \varphi^* \le \pi)$. They result in

$$\frac{\varepsilon}{\varepsilon'} = 1 + \frac{ac + bd}{2}. \quad (26)$$

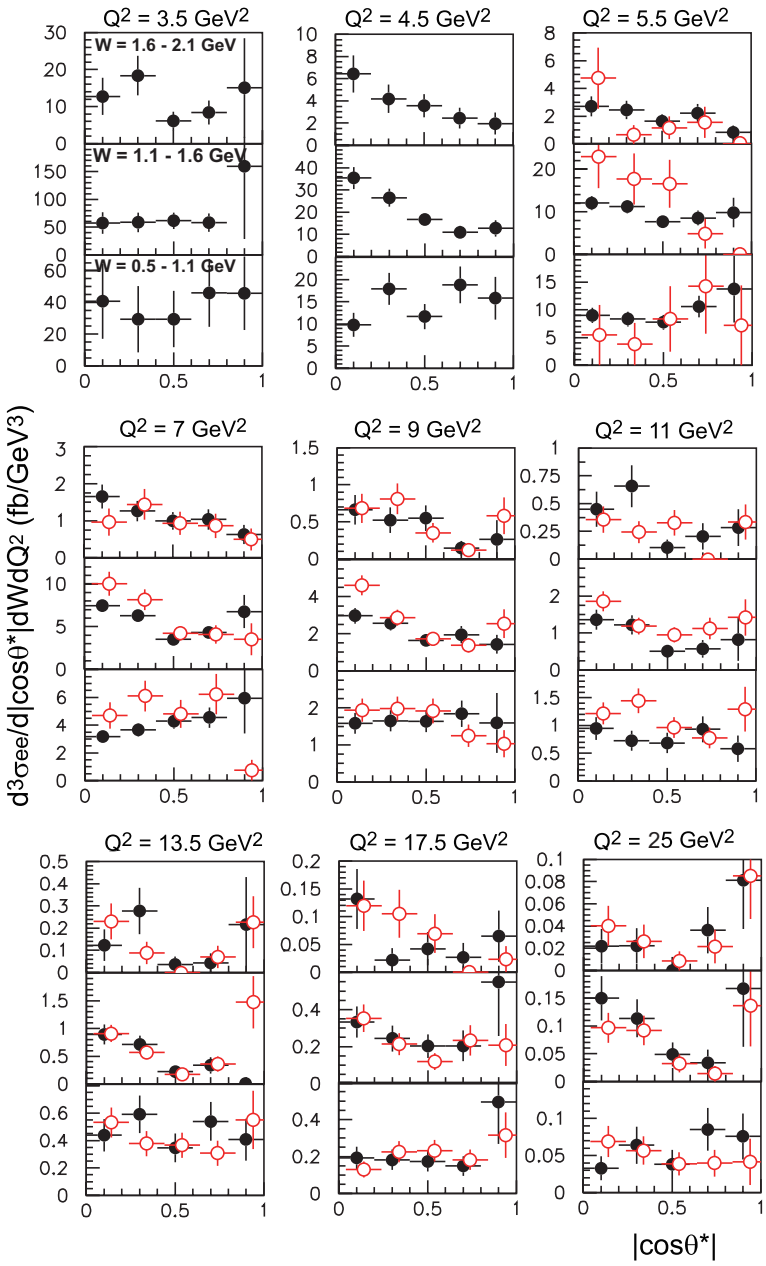

FIG. 19: The $|\cos\theta^*|$ dependence of the e^+e^--based cross section in each Q^2 bin. The dependence for three different W regions is shown in above each panel, and the W regions are 0.5 – 1.1 GeV, 1.1 – 1.6 GeV, 1.6 – 2.1 GeV from bottom to top within each panel, as indicated in the upper left panel. The closed circles (open circles) are for the e-tag (p-tag) measurements. The plotting location for each p-tag point is shifted slightly to improve the visibility of the error bars. The efficiency corrections and background subtraction are applied.

This formula is independent of the normalizations of the $N_{\rm MC}(\varphi^*)$ and $N_{\rm EXP}(\varphi^*)$ functions. We approximate $N_{\rm MC}(\varphi^*)$ with a Fourier expansion up to $\cos 4\varphi^*$; the coefficients of $\cos 3\varphi^*$ and $\cos 4\varphi^*$ terms do not affect the ε/ε' result because $P(\varphi^*)$ is up to only $\cos 2\varphi^*$, but the effect of the terms is significant in the fit to determine the coefficients c and d. The φ^* dependence of the efficiency and the fit for two W regions in the Q^2 range between 8 GeV^2 and 12 GeV^2 is shown in Fig. 20. The experimen-

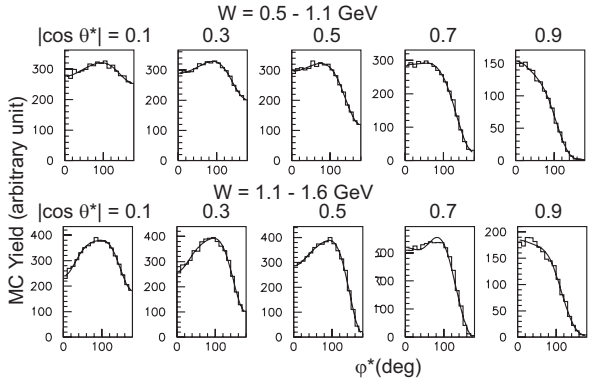

FIG. 20: The φ^* distributions for $\varepsilon(\varphi^*) \propto N_{\rm MC}(\varphi^*)$ for the W region 0.5 – 1.1 GeV (upper row) and 1.1 – 1.6 GeV (lower row), and 8 GeV^2 $< Q^2 <$ 12 GeV^2. They are separately plotted for the five angular regions, whose central $|\cos\theta^*|$ value is indicated in each panel. The solid curve is the fit to the Fourier expansion described in the text.

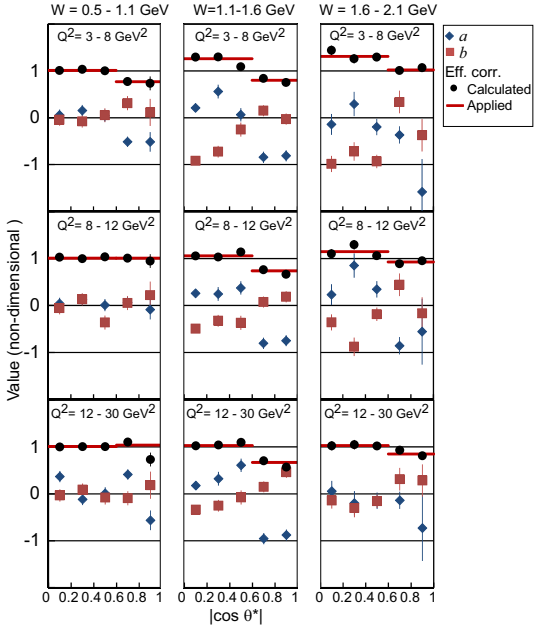

FIG. 21: The $|\cos\theta^*|$ dependence of the obtained parameters of a, b, and the efficiency correction factor ε/ε'; a and b are the coefficients of $\cos\varphi^*$ and $\cos 2\varphi^*$ in $P(\varphi^*)$ for each of the nine (W, Q^2) regions (see the text). Thick lines indicate the efficiency correction factor, which is applied to obtain the φ^*-integrated cross section.

tal results for the φ^*-differentiated cross section are discussed in Sec. VII C.

We find that the φ^* dependence of the differential cross section, and thus the correction-factor value, change drastically between above and below $|\cos\theta^*| = 0.6$ and that the value for each of $|\cos\theta^*| < 0.6$ and $|\cos\theta^*| > 0.6$ is almost constant for the cells with the same (W, Q^2). Thus, we take a weighted average of the correction factor for the three (two) bins of $|\cos\theta^*| < 0.6$ ($|\cos\theta^*| > 0.6$), in order to reduce the uncertainty of the correction. The obtained efficiency correction factor ε/ε', as well as the fit results for a and b, are plotted in Fig. 21. The correction factor ranges from 0.67 to 1.31 and is within 0.93 – 1.06 for 10 of the 18 regions.

The trend of the φ^* dependence is explained by the interference term(s) with the D_0 ($J = 2$ and $\lambda = 0$) component, which changes its sign at $1/\sqrt{3}$ (≈ 0.577) according to the Y_2^0 function (see Eq. (29)).

D. Radiative correction and Q^2 unfolding

We apply a correction of 2% ($\delta = 0.02$) for the cross section as the radiative correction. This is the same as that evaluated in the single pion production [10]. This correction depends very little on W, $|\cos\theta^*|$, and Q^2, and is treated as a constant.

We define the nominal Q^2 for each bin with a finite bin width, $\bar{Q}^2$, using the formula

$$\frac{d\sigma_{ee}}{dQ^2}(\bar{Q}^2) = \frac{1}{\Delta Q^2}\int_{\rm bin}\frac{d\sigma_{ee}}{dQ^2}(Q^2)dQ^2, \qquad (27)$$

TABLE IV: The nominal Q^2 value ($\bar{Q}^2$) for each Q^2 bin.

Q^2 bin (GeV^2)	Bin center (GeV^2)	$\bar{Q}^2$ (GeV^2)
3 – 4	3.5	3.45
4 – 5	4.5	4.46
5 – 6	5.5	5.47
6 – 8	7.0	6.89
8 – 10	9.0	8.92
10 – 12	11.0	10.93
12 – 15	13.5	13.37
15 – 20	17.5	17.23
20 – 30	25.0	24.25

where ΔQ^2 is the bin width. We assume an approximate dependence of $d\sigma/dQ^2 \propto Q^{-7}$ for the calculation [10], independent of W and $|\cos\theta^*|$, and have omitted the notations of W and $|\cos\theta^*|$ in Eq. (27). The $\bar{Q}^2$ values for the Q^2 bins are listed in Table IV. We use the luminosity function at this $\bar{Q}^2$ point to obtain the $\gamma^*\gamma$-based cross section for each Q^2 bin. We also use the central value of the Q^2 bins to represent the individual bins in tables and figures for convenience of description.

The Q^2 value measured for each event differs from the true Q^2 for two reasons: the resolution effect of the Q^2 determination and the reduction of the incident electron energy due to ISR.

The signal yield is measured in bins of reconstructed $Q^2_{\rm rec}$. For the true value of Q^2, we use the corrected value $Q^2_{\rm cor}$, and we assign the number in $Q^2_{\rm cor}$ for each of the measurement bins. According to the ISR effect found in the signal-MC events, $Q^2_{\rm rec}$ is about 1% larger than $Q^2_{\rm cor}$ on average. We estimate the displacement of events across bins using the signal-MC events in order to unfold the Q^2 distributions folded by the displacement.

We correct the measurement by the factor $f_i = \sum_j N_{ji}/\sum_j N_{ij}$, following the method applied to the Q^2 edge regions in our previous analysis for π^0-TFF [10], where N_{ij} is the transfer matrix obtained from MC simulation with the adjusted Q^2-dependence close to the observed dependence; here i (j) is the bin number for $Q^2_{\rm rec}$ ($Q^2_{\rm cor}$).

However, the correction for this Q^2 migration effect is already partially included in the efficiency determination. We have defined the efficiency as the selected number of events in a $Q^2_{\rm rec}$ bin, as in the experimental data, but divided by the number of generated events in the $Q^2_{\rm cor}$ bin. This is due to the difficulty to define $Q^2_{\rm rec}$ for generated events falling outside the detector acceptance. Thus, a migration effect is also introduced in the efficiency, but more weakly than in the experimental data, at half the size of the latter, due to the different Q^2 dependencies. By the consideration of this point, we correct the cross section for this effect by the factor $(f_i - 1)/2$ and assign a systematic uncertainty of the same size as the correction value. The correction is +5% for the lowest Q^2 bin and within ±3% for the other Q^2 bins. We assign the systematic uncertainty for this correction with about half the size of the correction, 2%.

We do not use the matrix inversion unfolding method [10] because the low statistics in the related multidimensional bins would tend to enhance the statistical errors. In addition, a systematic bias could appear in the edge bins of the measured Q^2 range by this method.

The measured $\gamma^*\gamma$-based cross section $\sigma_{\gamma*\gamma} = \sigma_{\rm TT} + \epsilon_0\sigma_{\rm LT} \equiv \sigma$ is discussed and shown in figures in Sec. VII.

TABLE V: Value of the ϵ_0 parameter depending on Q^2 for the two W regions.

	W region	
Q^2 bin (GeV^2)	0.5 – 1.6 GeV	1.6 – 2.1 GeV
3 – 4	0.82	0.77
4 – 5	0.88	0.84
5 – 6	0.90	0.83
6 – 8	0.89	0.83
8 – 10	0.88	0.85
10 – 12	0.88	0.85
12 – 15	0.86	0.83
15 – 20	0.82	0.80
20 – 30	0.76	0.73

E. Effect of $\sigma_{\rm LT}$ (helicity-1) component in the signal sample

We estimate ϵ_0, the factor multiplying $\sigma_{\rm LT}$ in Eq. (12), in each bin. We use the mean value of ϵ_0 calculated by Eq. (8) for each selected event from the signal-MC samples in different kinematical regions. The value of ϵ_0 has a weak dependence on Q^2, W, $|\cos\theta^*|$, and φ^*. Since the W dependence, in W = 0.5 – 1.5 GeV and the $|\cos\theta^*|$ dependence are small (within ±4%), we neglect their effect. It has some φ^* dependence (up to ±7%).

We have compared the Q^2 dependence of the experimental events with that of the signal-MC samples and have confirmed their consistency. Similar calculations for ϵ_1 are also performed.

We tabulate the Q^2 dependence of ϵ_0 in Table V for the two W regions. The expected values are $\epsilon_0 = 0.88 \pm 0.06$ and $\epsilon_1 = 1.28 \pm 0.07$ for W = 1.1 – 1.5 GeV for the Q^2-integrated samples. The ranges in ε_1 and ε_2 are due to the φ^* dependence. These values are used for partial-wave analyses performed with Q^2-dependent and Q^2-integrated cross sections in Sec. VII C and VII D, respectively.

For a quantitative study of the $\lambda = 1$ component, we use the azimuthal-angle differentiated cross section $d^2\sigma/d|\cos\theta^*|d\varphi^*$. It is derived as follows.

The φ^* dependence of $d^2\sigma/d|\cos\theta^*|d\varphi^*$ follows $N_{\rm EXP}(\varphi^*)/N_{\rm MC}(\varphi^*)$ in each W and $|\cos\theta^*|$ bin integrated in the Q^2 = 5 – 30 GeV^2 region. For this purpose, we use five W bins, 0.7 – 1.1 GeV, 1.1 – 1.2 GeV, 1.2 – 1.3 GeV, 1.3 – 1.4 GeV, and 1.4 – 1.5 GeV.

The φ^* dependence is normalized to the arithmetic mean $\langle d\sigma/d|\cos\theta^*|\rangle$ of the differential cross section

over the corresponding (W, Q^2) bins. We do not use the results for $Q^2 < 5$ GeV^2 because poor statistics in that region would diminish the accuracy of the arithmetic mean.

The normalization results in

$$\int_0^\pi \frac{d^2\sigma}{d|\cos\theta^*|d\varphi^*} d\varphi^* = \langle \frac{d\sigma}{d|\cos\theta^*|} \rangle. \qquad (28)$$

The results for $d^2\sigma/d|\cos\theta^*|d\varphi^*$ are shown in Sec. VII.

F. Systematic uncertainties

We estimate systematic uncertainties in the measurement of the differential cross section; these are summarized in Table VI.

1. *Uncertainties for the efficiency evaluation*

The detection efficiency is evaluated using the signal-MC events. However, the simulation has some errors or ambiguities in the reproduction of detector performance. This translates into uncertainties in the efficiency evaluation.

Tracking has a 1% uncertainty, which is estimated from a study of the decays $D^{*\pm} \to D^0\pi^\pm, D^0 \to K^0_S(\to \pi^+\pi^-)\pi^+\pi^-$ (0.35% per track) as well as an uncertainty of the radiation by an electron within the CDC volume.

The electron identification efficiency in this measurement is very high, around 98%, and a 1% systematic uncertainty is assigned for this term. Detection of the $\gamma\gamma$ pair for reconstructing $\pi 1$ has a 3% uncertainty. The mass resolution of $\pi 1$ is well reproduced in the MC simulation but the selection with the invariant mass introduces an additional 3% uncertainty, according to a comparison of the mass distributions between the MC and data samples. The $\pi 2$ reconstruction has a 3% uncertainty also. The uncertainty of the π^0 reconstruction efficiency is estimated by a comparison of the yields of D^0 to $K^\mp\pi^\pm$ and $K^\mp\pi^\pm\pi^0$ decays. We combine the two uncertainties for $\pi 1$ in quadrature (then 4.2% for $\pi 1$) and add the uncertainty for $\pi 2$ to it linearly, because the uncertainties for the two pions are fully correlated: the overall uncertainty is 7.2% for the two pions.

A kinematical condition using $E_{\rm ratio}$ applied in the selection gives an uncertainty of 2%. In addition, ambiguities in the detector edge locations and other geometrical-definition effects cause an uncertainty of 2%.

The uncertainty from the trigger efficiency is estimated by changing the energy thresholds of the Bhabha-veto in the HiE trigger (1%) and the cluster energy of the Clst4 trigger (2%), as performed in our previous analyses [10, 28, 29]. The estimation methodology is the same but the effects are different among the different processes. The total uncertainty for the trigger efficiency is 3%.

Background tracks and photons overlapping with the signal events may reduce the efficiency; this effect is accounted in MC by embedding the non-triggered event pattern (random trigger) in the signal. We estimate this effect by investigating the background conditions during different beam conditions or run periods. The effect on the efficiency is estimated to be 2%. The largest effect for the present analysis is estimated to come from background photons that form an extra π^0 with another true or background photon.

We take into account an uncertainty for the efficiency-correction factor arising from the φ^* dependence. Half of the difference of the factors in the two neighboring Q^2 regions is assigned to the uncertainty for each (W,$|\cos\theta^*|$) region for the evaluation. We choose the larger for the 8 GeV^2 $< Q^2 <$ 12 GeV^2 regions, where two neighboring Q^2 regions exist. The systematic error ranges from 1% to 16%, according to strength of the Q^2 dependence of the factor.

2. *Uncertainties from the background subtraction*

We take into account the backgrounds from the single π^0 production process and the virtual Compton process. We do not perform any qualitative simulation for the latter process and use only an estimate based on the features found in the experimental data. We assign the subtraction size applied for these two background sources as the systematic uncertainty for $|\cos\theta^*| > 0.9$. In addition, we assign another 1% error, added linearly, from the same sources for all the angular bins.

We assign half of the subtraction size as the uncertainty of the background subtractions for the $\gamma\pi^0$ production and non-exclusive processes; they are estimated using the signal and background MC and/or the experimental sideband events.

We add the systematic uncertainty from the latter backgrounds in quadrature, but the others linearly, because the first three have a common feature that photon(s) and pion(s) are from backgrounds. The last one is different: some particles escape detection.

The total uncertainty in the background subtraction ranges from 1% to 23%, depending on the (W,

$|\cos\theta^*|$, Q^2) bin. The error is relatively large for the forward angles in the lowest W or the higher Q^2 regions.

3. Uncertainties from other sources

The unfolding procedure has an uncertainty of 2%. The radiative correction has an uncertainty of 3%. The evaluation of the luminosity function gives an uncertainty of 4%, including a model uncertainty for the form factor of the untagged side (2%). This model uncertainty is based on the difference of the product of the luminosity function and efficiency between the two models: one with $\sim 1/(1+Q_2^2/m_\rho^2)$ and the other constant in Q_2^2 (effectively the same as the model with a dependence of $\sim 1/(Q_1^2+Q_2^2)^d$ because $Q_2^2 \ll Q_1^2$, where d is a power parameter representing the high-Q_1^2 behavior). The integrated luminosity has a measurement uncertainty of 1.4%.

The systematic uncertainties are added in quadrature unless noted above. The total systematic uncertainty is between 11% and 26%, depending on the (W, $|\cos\theta^*|$, Q^2) bin.

In the following analysis, we treat a 4% systematic uncertainty — from the kinematical cut, geometrical acceptance and partially from the trigger efficiency and unfolding for Q^2 — a bin-by-bin error that distorts the W dependence. We also take into account the systematic uncertainty in the efficiency correction from φ^* dependence, which distorts the $|\cos\theta^*|$ dependence. The remaining part is treated as an uncertainty of the overall normalization.

TABLE VI: Sources of systematic uncertainties. The values indicated in a range show the range sizes in different bins.

Source	Uncertainty (%)
Tracking	1
Electron-ID	1
Pion-pair detection (for two π^0's)	7.2
Kinematical selection	2
Geometrical acceptance	2
Trigger efficiency	3
Background effect for the efficiency	2
φ^* dependence	1 – 16
Background subtraction	1 – 23
Unfolding for Q^2	2
Radiative correction	3
Luminosity function	4
Integrated luminosity	1.4
Total	11 – 26

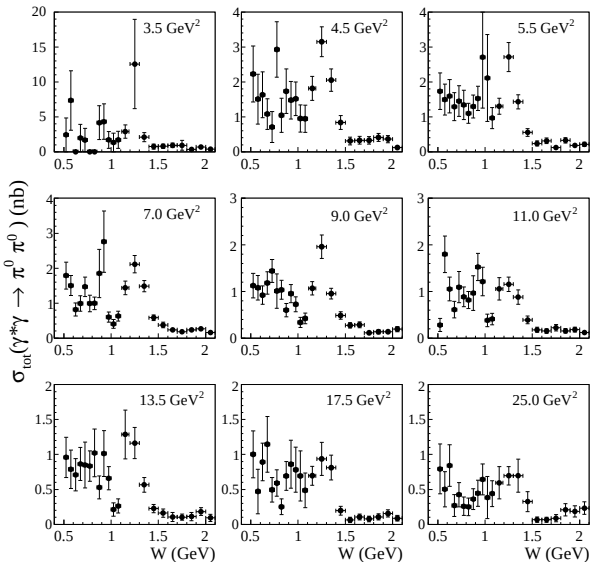

FIG. 22: Integrated cross section for $\gamma^*\gamma \to \pi^0\pi^0$ in nine Q^2 bins in GeV^2 indicated in each panel.

VII. MEASUREMENT OF TRANSITION FORM FACTORS

Figure 22 shows the integrated cross section as a function of W for the process $\gamma^*\gamma \to \pi^0\pi^0$ in nine Q^2 bins. Peaks corresponding to the $f_2(1270)$ and $f_0(980)$ are evident. In this section, we extract the Q^2 dependence of the TFF of the $f_0(980)$ and those of the helicity-0, -1, and -2 components of the $f_2(1270)$.

A. Partial-wave amplitudes

Helicity amplitudes in Eq. (11) are functions of W, Q^2, and θ^* but not of φ^* [14] and can be expanded in terms of partial waves. In this channel, only even angular-momentum partial waves contribute. Furthermore, in the energy region $W \le 1.5$ GeV, $J > 2$ partial waves (the next having $J = 4$) may be neglected so that only S and D waves need be considered. Then, Eqs. (5) to (7) can be written as

$$\begin{aligned} t_0 &= |SY_0^0 + D_0 Y_2^0|^2 + |D_2 Y_2^2|^2 + 2\epsilon_0 |D_1 Y_2^1|^2, \\ t_1 &= 2\epsilon_1 \Re\left((D_2^* |Y_2^2| - S^* Y_0^0 - D_0^* Y_2^0) D_1 |Y_2^1|\right), \\ t_2 &= -2\epsilon_0 \Re\left(D_2^* |Y_2^2| (S Y_0^0 + D_0 Y_2^0)\right), \end{aligned} \quad (29)$$

where S is the S-wave amplitude, D_0, D_1, and D_2 denote the helicity-0, -1, and -2 components of the D wave, respectively [30], and Y_J^m are the spherical harmonics:

$$\begin{aligned} Y_0^0 &= \sqrt{\frac{1}{4\pi}}\,, \\ Y_2^0 &= \sqrt{\frac{5}{16\pi}}(3\cos^2\theta^* - 1)\,, \\ |Y_2^1| &= \sqrt{\frac{15}{8\pi}}\sin\theta^*\cos\theta^*\,, \\ |Y_2^2| &= \sqrt{\frac{15}{32\pi}}\sin^2\theta^*\,. \end{aligned} \tag{30}$$

We take the absolute values of the spherical harmonics because the helicity amplitudes do not have φ^* dependence [14]. When integrated over the azimuthal angle, the differential cross section can then be expressed as

$$\begin{aligned} &\frac{d\sigma(\gamma^*\gamma \to \pi^0\pi^0)}{4\pi d|\cos\theta^*|} = \left|S\,Y_0^0 + D_0\,Y_2^0\right|^2 \\ &+2\epsilon_0\left|D_1\,Y_2^1\right|^2 + \left|D_2\,Y_2^2\right|^2. \end{aligned} \tag{31}$$

The angular dependence of the cross section is governed by the spherical harmonics, while the W and Q^2 dependencies are determined by the partial waves.

B. Parameterization of amplitudes

The $f_0(980)$ and the $f_2(1270)$ have been clearly observed in no-tag $\pi^0\pi^0$ production [28]. The signal is visible in the Q^2-integrated spectrum (Fig. 6) as well as in most of the Q^2 bins in Fig. 22. Motivated by this, we try to extract the Q^2 dependence of the TFFs: $F_{f2}(Q^2)$ of the $f_2(1270)$ together with its helicity-0, -1, and -2 components and $F_{f0}(Q^2)$ of the $f_0(980)$. This is done by parameterizing S, D_0 (and/or D_1), and D_2 and by fitting the data in the energy region 0.7 GeV $\leq W \leq$ 1.5 GeV.

S and D_i ($i = 0, 1, 2$) are parameterized as follows (considering the general case where the φ^*-dependent cross section is to be fitted):

$$\begin{aligned} S &= A_{f_0(980)}e^{i\phi_{f0}} + B_S e^{i\phi_{BS}}, \\ D_i &= \sqrt{r_i(Q^2)}A_{f_2(1270)}e^{i\phi_{f2Di}} + B_{Di}e^{i\phi_{BDi}} \end{aligned} \tag{32}$$

where $A_{f_0(980)}$ and $A_{f_2(1270)}$ are the amplitudes of the $f_0(980)$ and $f_2(1270)$, respectively; $r_i(Q^2)$ is the fraction of the $f_2(1270)$-contribution in the D_i wave with the constraints $r_0 + r_1 + r_2 = 1$ and $r_i \geq 0$; B_S and B_{Di} are non-resonant "background" amplitudes for the S and D waves; ϕ_{BS}, ϕ_{BDi}, ϕ_{f0} and ϕ_{f2Di} are the phases of background amplitudes (S and D_i), the $f_0(980)$ and $f_2(1270)$ in the D waves, respectively. The phases are assumed to be independent of Q^2. The contributions of the $f_2'(1525)$ and $f_0(Y)$ (that are included in no-tag $\pi^0\pi^0$ production [28]) are neglected. The overall arbitrary phase is fixed by taking $\phi_{f2D2} = 0$. When fitting the φ^*-integrated cross section, we also set $\phi_{BS} = \phi_{BD1} = 0$.

A power behavior in W is assumed for the background amplitudes, which are multiplied by the threshold factor β^{2l+1} (l denoting the orbital angular momentum of the two-π^0 system) with an assumed Q^2 dependence for all the waves:

$$\begin{aligned} B_S &= \frac{\beta a_S\,(W_0/W)^{b_S}}{(Q^2/m_0^2+1)^{c_S}}\,, \\ B_{D0} &= \frac{\beta^5 a_{D0}\,(W_0/W)^{b_{D0}}}{(Q^2/m_0^2+1)^{c_{D0}}}\,, \\ B_{D1} &= \frac{\beta^5 Q^2 a_{D1}\,(W_0/W)^{b_{D1}}}{(Q^2/m_0^2+1)^{c_{D1}}}\,, \\ B_{D2} &= \frac{\beta^5 a_{D2}\,(W_0/W)^{b_{D2}}}{(Q^2/m_0^2+1)^{c_{D2}}}\,. \end{aligned} \tag{33}$$

Here, $\beta = \sqrt{1 - 4m_{\pi^0}^2/W^2}$ is the velocity of π^0 divided by the speed of light, m_{π^0} is the π^0 mass, and W_0 and m_0 are assigned the values 1.1 GeV and 1.0 GeV/c^2, respectively. Note that B_{D1} has an additional factor of Q^2 to ensure that the amplitude becomes zero at $Q^2 = 0$. We set $a_i \geq 0$ ($i = S, D_0, D_1, D_2$) to fix the arbitrary sign of each background amplitude (by absorbing the sign into their corresponding phases). We allow b_i to have a negative sign because amplitudes may still be an increasing function of W, but we limit $|b_i| < 5$; large b_i values give a rapid W dependence, which is considered unphysical.

We use the parameterizations of the $f_0(980)$ and $f_2(1270)$ given in Refs. [31, 32] that are multiplied by their TFFs to allow a Q^2 dependence. Note that $\mathcal{B}(f_J \to \pi^0\pi^0)/\mathcal{B}(f_J \to \pi^+\pi^-) = 1/2$ (because the f_J mesons are isoscalar). For completeness, we reproduce here the parameterization of the $f_0(980)$ and the $f_2(1270)$. For the $f_0(980)$ meson, we need to take into account the fact that its mass is close to the $K\bar{K}$ threshold. The parameterization we adopt is

$$A_{f_0(980)} = F_{f0}(Q^2)\sqrt{1 + \frac{Q^2}{M_{f_0}^2}}\,\frac{\sqrt{8\pi\beta_\pi}}{W}\,\frac{g_{f_0\gamma\gamma}g_{f_0\pi\pi}}{16\sqrt{3}\pi}\,\frac{1}{D_{f_0}}, \tag{34}$$

where $F_{f0}(Q^2)$ is the transition form factor of the $f_0(980)$, $\sqrt{1+Q^2/M_{f_0}^2}$ is the flux factor that arises from definition of the luminosity function for a tagged two-photon cross section, $\beta_X = \sqrt{1-4{M_X}^2/W^2}$ is the velocity divided by the speed of light for a particle X with mass M_X in the two-body final states, and g_{f_0XX} is related to the partial width of the $f_0(980)$ meson via $\Gamma_{XX}(f_0) = \beta_X g_{f_0XX}^2/(16\pi M_{f_0})$. The factor D_{f_0} is given by the following expression [33]:

$$\begin{aligned} D_{f_0}(W) &= M_{f_0}^2 - W^2 + \Re\Pi_\pi^{f_0}(M_{f_0}) - \Pi_\pi^{f_0}(W) \\ &\quad + \Re\Pi_K^{f_0}(M_{f_0}) - \Pi_K^{f_0}(W), \end{aligned} \tag{35}$$

with

$$\Pi_X^{f_0}(W) = \frac{\beta_X g_{f_0XX}^2}{16\pi}\left[i + \frac{1}{\pi}\ln\frac{1-\beta_X}{1+\beta_X}\right], \tag{36}$$

where $X = \pi$ or K. The factor β_K is real in the region $W \geq 2M_K$ and becomes imaginary for $W < 2M_K$. The parameter values are summarized in Table VII.

TABLE VII: Parameters of the $f_0(980)$ used in the fit. When two errors are provided, the first is statistical, and the second systematic.

Parameter	Value	Reference
Mass (MeV/c^2)	980 ± 20	[34]
$g_{f_0(980)\pi\pi}$(GeV)	$1.82 \pm 0.03\ ^{+0.24}_{-0.17}$	[28]
$\Gamma_{\gamma\gamma}$(keV)	$0.29\ ^{+0.07}_{-0.06}$	[34]
$g_{f_0K\bar{K}}^2/g_{f_0\pi\pi}^2$	$4.21 \pm 0.25 \pm 0.21$	[35]

We use a parameterization of the $f_2(1270)$ in Ref. [28] multiplied by the TFF, $F_{f2}(Q^2)$. The relativistic Breit-Wigner resonance amplitude $A_R(W)$ for a spin-J resonance R of mass m_R is given by

$$\begin{aligned} A_R^J(W) &= F_R(Q^2)\sqrt{1+\frac{Q^2}{M_R^2}}\sqrt{\frac{8\pi(2J+1)m_R}{W}} \\ &\quad \times \frac{\sqrt{\Gamma_{\rm tot}(W)\Gamma_{\gamma\gamma}(W)\mathcal{B}(\pi^0\pi^0)}}{m_R^2 - W^2 - im_R\Gamma_{\rm tot}(W)}, \end{aligned} \tag{37}$$

where $F_R(Q^2)$ is the TFF of the resonance R and $\sqrt{1+Q^2/M_R^2}$ is the flux factor mentioned above. Hereinafter, we consider the case $J = 2$. The energy-dependent total width $\Gamma_{\rm tot}(W)$ is given by

$$\Gamma_{\rm tot}(W) = \sum_X \Gamma_{X\bar{X}}(W) + \Gamma_{\rm other}(W), \tag{38}$$

TABLE VIII: Parameters of the $f_2(1270)$.

Parameter	$f_2(1270)$	Reference
Mass (MeV/c^2)	1275.1 ± 1.2	[34]
$\Gamma_{\rm tot}$ (MeV)	$185.1^{+2.9}_{-2.4}$	[34]
$\mathcal{B}(\pi\pi)$ (%)	$84.8^{+2.4}_{-1.2}$	[34]
$\mathcal{B}(K\bar{K})$ (%)	4.6 ± 0.4	[34]
$\mathcal{B}(\eta\eta)$ (%)	0.40 ± 0.08	[34]
$\mathcal{B}(\gamma\gamma)$ (10^{-6})	16.4 ± 1.9	[34]
r_R ((GeV/c)$^{-1}$)	3.62 ± 0.03	[32]

where X is π, K, η, γ, etc. For $J = 2$, the partial width $\Gamma_{X\bar{X}}(W)$ is parameterized as [36]

$$\begin{aligned} \Gamma_{X\bar{X}}(W) &= \Gamma_R\mathcal{B}(R\to X\bar{X})\left(\frac{q_X(W^2)}{q_X(m_R^2)}\right)^5 \\ &\quad \times \frac{D_2\left(q_X(W^2)r_R\right)}{D_2\left(q_X(m_R^2)r_R\right)}, \end{aligned} \tag{39}$$

where Γ_R is the total width at the resonance mass,

$$\begin{aligned} q_X(W^2) &= \sqrt{\frac{W^2}{4} - m_X^2}, \\ D_2(x) &= \frac{1}{9+3x^2+x^4}, \end{aligned} \tag{40}$$

and r_R is an effective interaction radius that varies from 1 (GeV/c)$^{-1}$ to 7 (GeV/c)$^{-1}$ in different hadronic reactions [37]. For the three-body and other multi-body decay modes,

$$\Gamma_{\rm other}(W) = \Gamma_R\mathcal{B}(R\to{\rm other})\frac{W^2}{m_R^2} \tag{41}$$

is used instead of Eq. (39). All parameters of the $f_2(1270)$ are fixed at the PDG values [34] except for r_R, which is fixed at the value determined in Ref. [32], as summarized in Table VIII.

The normalizations of TFFs are such that $F_{f0}(0) = 1.00 \pm 0.11$ and $F_{f2}(0) = 1.00 \pm 0.06$; the errors reflect the uncertainties of the two-photon decay widths (at $Q^2 = 0$) of the $f_0(980)$ and $f_2(1270)$ [34]. The TFF of the $f_2(1270)$ for the helicity-i component is given by $\sqrt{r_i(Q^2)}F_{f2}(Q^2)$, according to Eq. (32).

Here, we note that there is a limitation in the partial-wave analysis based on Eq. (31) (*i.e.*, through the φ^*-integrated cross section). That is, we can extract information on partial waves for three out of the four (S, D_0, D_1, and D_2) waves only. This can

be understood from the fact that Eq. (31) can be written as a function of $z \equiv |\cos\theta^*|$ as $a + bz^2 + cz^4$, *i.e.*, only three coefficients a, b, c are independent, where a, b, c are given by combinations of the S, D_0, D_1, and D_2 waves. This conclusion holds whether or not the interference term $\Re(S^* D_0)$ exists.

To partially overcome this limitation, we first fit the φ^*-dependent (but Q^2-integrated) differential cross section in Sec. VII C, to obtain information on the fractions of the $f_2(1270)$ in the D_0, D_1, and D_2 waves. Then in Sec. VII D, this information is used in the fit of the φ^*-integrated cross section.

C. Analysis of the φ^*-dependent cross section

As described above, the φ^*-integrated cross section does not give information on all the partial waves (S, D_0, D_1, and D_2). Here, we analyze the φ^*-dependent cross section to partially overcome this problem. Because of limited statistics, the φ^*-dependent cross section is integrated over Q^2; it is divided into nine φ^* bins with a bin width of 20°, five equal-width $|\cos\theta^*|$ bins, and five W bins of 0.7 – 1.1 GeV, 1.1 – 1.2 GeV, 1.2 – 1.3 GeV, 1.3 – 1.4 GeV, and 1.4 – 1.5 GeV. The average value of $Q^2(Q^2_{\rm av})$ is 9.6 GeV^2. The cross section is fitted using the parameterization described above by ignoring the contribution of the $f_0(980)$ and Q^2 dependence. The values of ϵ_0 and ϵ_1 are evaluated at $Q^2_{\rm av}$.

Parameters describing the assumed amplitudes are obtained by minimizing χ^2. To search for the true minimum and to identify possible multiple solutions, 1000 sets of randomly generated initial parameters are employed for fits performed using MINUIT [39]. Fitted values are accepted as satisfactory solutions when their χ^2 values are within $\chi^2_{\rm min} + 10$ (corresponding to 3.2σ), where $\chi^2_{\rm min}$ is the χ^2 value at the true minimum.

There are too many parameters to be fitted simultaneously, particularly from the non-resonant (background) amplitude that interferes with the resonant one in each wave. Thus we study the sensitivity of parameters especially in the D waves by investigating several sets of assumptions in the parameters.

Two categories of fits are made: $B_{D2} \neq 0$ and $B_{D2} = 0$, because we consider that the interference between the $f_2(1270)$ and a possible non-resonant background is important in the D_2 wave. In each category, we try cases where both r_0 and r_1 are non-zero or one of them is zero in Eq. (32). The number of solutions found is one or two as listed in Table IX. Here, solutions in which any of powers (b's) in Eq. (33) exceed 5 are discarded as unphysical provided that the corresponding a parameter is not consistent with zero.

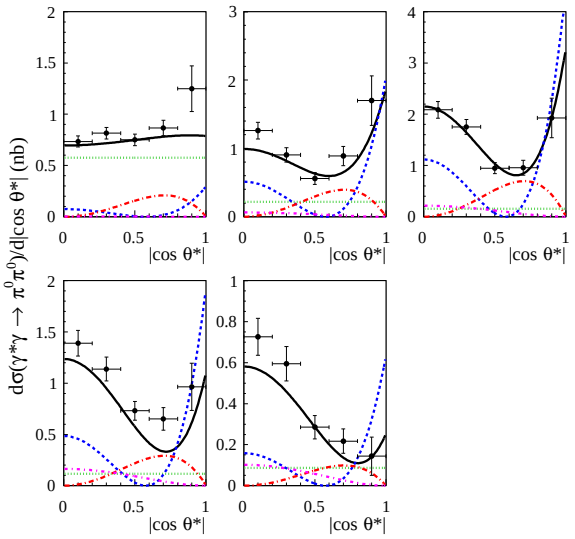

FIG. 23: $|\cos\theta^*|$ dependence in five W bins: 0.9, 1.15, 1.25, 1.35, and 1.45 GeV from left to right and top to bottom and fitted results of the φ^* nominal fit. Legend of lines are: solid lines show the total (black), dotted $|S|^2$ (green), dashed $|D_0|^2$ (blue), long dashed $|D_1|^2$ (red), and dash-dotted $|D_2|^2$ (purple).

Two solutions are obtained for $B_{D2} \neq 0$ where neither r_0 nor r_1 is zero. The favored solution that has a smaller χ^2 (referred to as a "φ^* nominal fit") has a small B_{D2}, which naturally gives almost identical values with respect to the fit with $B_{D2} = 0$. The fitted values of $F_{f2}(Q^2_{\rm av})$ are rather similar for all the fits. The fitted fraction of the $f_2(1270)$ in the D_0 wave (r_0) is large; the assumption of $r_0 = 0$ is disfavored as it gives a much worse χ^2. If, in addition, r_1 is fitted, the obtained value is $r_1 = 0.15^{+0.05}_{-0.03}$ for the φ^* nominal fit, whose value is used in the "r_1 fit" described in Sec. VII D. In the second solution, B_{D2} interferes destructively with the $f_2(1270)$ giving a smaller value of $r_1 = 0.11 \pm 0.03$. Figures 23 – 27 show the fitted results of the φ^* nominal fit that are projected onto the variable plotted and integrated over the other variables.

TABLE IX: Fitted parameters of the φ^*-dependent cross section. Here, $Q^2_{\rm av} = 9.6$ GeV^2.

Parameter	$B_{D2} \neq 0$				$B_{D2} = 0$			
condition	$r_0 \neq 0 \bigcap r_1 \neq 0$		$r_0 = 0$	$r_1 = 0$	$r_0 \neq 0 \bigcap r_1 \neq 0$	$r_0 = 0$		$r_1 = 0$
No. sol.	2		1	1	1	2		1
	Sol.1	Sol.2				Sol.1	Sol.2	
χ^2/ndf	236.6/208	243.1/208	357.4/210	289.6/210	241.3/211	357.5/213	366.0/213	308.0/213
$F_{f2}(Q^2_{\rm av})(\times 10^{-2})$	1.67 ± 0.15	1.76 ± 0.11	$1.68^{+0.05}_{-0.06}$	1.46 ± 0.09	1.70 ± 0.08	$1.68^{+0.05}_{-0.06}$	1.65 ± 0.06	1.41 ± 0.06
a_{D2} ($\sqrt{\rm nb}$)	0.03 ± 0.03	$0.17^{+0.04}_{-0.05}$	0 ± 0.003	$0.23^{+0.02}_{-0.03}$	0 (fixed)			
b_{D2}	$-3.8^{+2.6}_{-8.8}$	$4.0^{+1.9}_{-1.0}$	-4.6 ± 7.9	$2.3^{+0.6}_{-0.5}$	–			
ϕ_{BD2} ($^\circ$)	89 ± 123	114^{+17}_{-16}	198 ± 1	101 ± 13	–			
r_0	0.76 ± 0.06	$0.80^{+0.04}_{-0.05}$	0 (fixed)	$0.81^{+0.06}_{-0.07}$	0.70 ± 0.04	0 (fixed)		$0.68^{+0.06}_{-0.07}$
a_{D0} ($\sqrt{\rm nb}$)	0.13 ± 0.03	$-0.13^{+0.04}_{-0.03}$	0.06 ± 0.02	0.15 ± 0.03	-0.13 ± 0.02	0.06 ± 0.02	$0.23^{+0.02}_{-0.03}$	0.16 ± 0.02
b_{D0}	$-1.0^{+0.9}_{-1.5}$	$-0.8^{+0.9}_{-1.4}$	$-1.5^{+1.3}_{-1.7}$	$-0.6^{+0.8}_{-1.1}$	$-0.6^{+0.8}_{-1.0}$	$-1.5^{+1.3}_{-1.7}$	$1.5^{+0.6}_{-0.4}$	-0.3 ± 0.6
ϕ_{BD0} ($^\circ$)	186^{+22}_{-22}	350 ± 21	300^{+18}_{-20}	161 ± 15	171 ± 12	300^{+18}_{-20}	271 ± 9	151^{+10}_{-9}
ϕ_{f2D0} ($^\circ$)	161^{+18}_{-18}	160^{+19}_{-16}	–	144^{+14}_{-13}	20 ± 12	–		184 ± 9
r_1	$0.15^{+0.05}_{-0.03}$	0.11 ± 0.03	$0.03^{+0.03}_{-0.02}$	0 (fixed)	0.16 ± 0.03	$0.03^{+0.03}_{-0.02}$	0.07 ± 0.04	0 (fixed)
a_{D1} ($\sqrt{\rm nb}$)	-0.11 ± 0.03	$0.15^{+0.02}_{-0.03}$	-0.09 ± 0.03	0.21 ± 0.01	-0.10 ± 0.02	0.09 ± 0.03	0.15 ± 0.02	0.17 ± 0.01
b_{D1}	$1.8^{+1.7}_{-1.7}$	$3.4^{+0.9}_{-0.7}$	$2.9^{+1.9}_{-1.3}$	$1.9^{+0.3}_{-0.2}$	$2.1^{+1.2}_{-1.1}$	$2.9^{+1.9}_{-1.3}$	$4.3^{+0.9}_{-0.9}$	$1.3^{+0.3}_{-0.3}$
ϕ_{BD1} ($^\circ$)	2 ± 5	225^{+21}_{-20}	166 ± 10	209 ± 17	140 ± 12	345 ± 10	356 ± 8	180 ± 9
ϕ_{f2D1} ($^\circ$)	148 ± 19	155^{+20}_{-19}	278 ± 29	–	163 ± 13	28^{+23}_{-36}	69^{+11}_{-21}	–
a_S ($\sqrt{\rm nb}$)	-0.30 ± 0.03	0.16 ± 0.02	0.29 ± 0.02	0.16 ± 0.02	0.30 ± 0.01	0.29 ± 0.02	0.18 ± 0.02	0.32 ± 0.01
b_S	2.0 ± 0.6	$-0.6^{+0.4}_{-0.5}$	$2.2^{+0.3}_{-0.3}$	$-0.1^{+0.4}_{-0.4}$	$1.9^{+0.2}_{-0.2}$	$2.2^{+0.3}_{-0.3}$	$0.6^{+0.4}_{-0.4}$	$1.4^{+0.2}_{-0.2}$
ϕ_{BS} ($^\circ$)	262 ± 19	73^{+15}_{-12}	76^{+6}_{-6}	60 ± 8	95^{+12}_{-11}	76^{+6}_{-6}	74 ± 7	80^{+8}_{-7}

D. Fitted results for the φ^*-integrated cross section

We fit the φ^*-integrated differential cross section, Eq. (11), in the W region 0.7 GeV $\leq W \leq$ 1.5 GeV for all Q^2 with Eq. (32) and Eq. (33). In the fit, the usual χ^2 is replaced by its corresponding quantity using the Poisson likelihood λ defined as [38]

$$\chi^2_{\rm P} \equiv \ln \lambda = 2 \sum_i \left[p_i - n_i + n_i \ln \left(\frac{n_i}{p_i} \right) \right], \quad (42)$$

where, n_i and p_i are the numbers of events observed and predicted in the i-th bin and the sum is over the bins within the fitted W range. We fit the predicted number of events in each bin that is related to the differential cross section. The latter is converted to the number of events by multiplying by a known conversion factor given from Eqs. (21) and (22). Here, we include zero-event bins in calculating $\chi^2_{\rm P}$ in Eq. (42). In fitting with Eq. (42), systematic uncertainties in the cross section are not taken into account. Their effects are considered separately in the study of systematic uncertainties in Sec. VII E.

The TFFs for the $f_0(980)$ and $f_2(1270)$ and the fractions $r_i(Q^2)$ are floated in each Q^2 bin, *i.e.*, $F_{f0}(Q^2)$, $F_{f2}(Q^2)$, and $r_i(Q^2)$ are obtained in each Q^2 bin.

Because of the limitation mentioned above, we cannot determine D_0 and D_1 simultaneously together with S and D_2.

Here, we prioritize the determination of D_0 and D_2 over D_1 by setting $B_{D1} = 0$ and

$$r_1(Q^2) = r_1(Q^2_{\rm av}) \left(\frac{Q^2}{Q^2_{\rm av}} \right)^d, \quad (43)$$

where $Q^2_{\rm av} = 9.6$ GeV^2 is the average Q^2 value for the Q^2-integrated cross section and $r_1(Q^2_{\rm av}) = 0.15$ determined in the φ^* nominal fit, and d is a free parameter. The effect of setting $B_{D1} = 0$ is considered in systematic studies. In this "r_1 fit," we can obtain information on the helicity-1 TFF simultaneously with those of helicity-0 and -2 in spite of the limitation.

The issue with the $f_2(1270)$ is determination of its fractions in D_0, D_1, and D_2 in each Q^2 bin. Thus, in addition to the r_1 fit, we perform fits assuming either $D_0 \neq 0$ with $D_1 = 0$ (denoted as the D_0 fit) or $D_1 \neq 0$ with $D_0 = 0$ (denoted as the D_1 fit). In each category, we put either $B_{D2} \neq 0$ or $B_{D2} = 0$. In the D_1 fit, the evaluation of ϵ_0 is necessary. It turns out that it has little dependence on W and $\cos\theta^*$ and we use the values listed in Table V for Q^2 bins from 3.5 to 25.0 GeV^2. We also use the average Q^2 value given in Table IV in each Q^2 bin in the fitting.

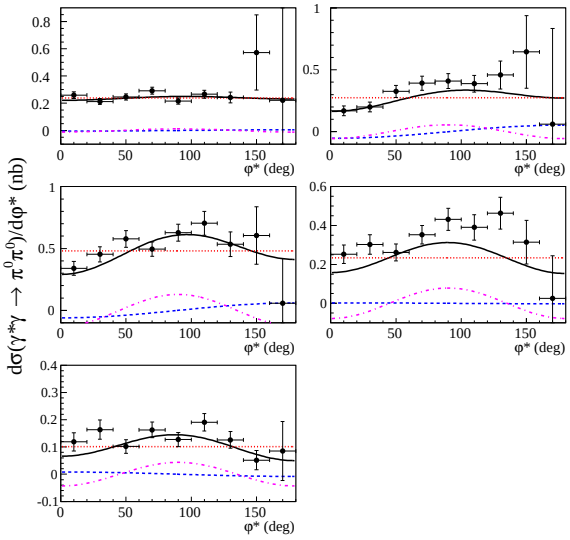

FIG. 24: φ^* dependence in five W bins: 0.9, 1.15, 1.25, 1.35, and 1.45 GeV from left to right and top to bottom and fitted results of φ^* nominal fit. Legend of lines: solid lines for the total (black), dotted t_0 (red), dashed $t_1 \cos\varphi^*$ (blue), and dash-dotted $t_2 \cos 2\varphi^*$ (purple).

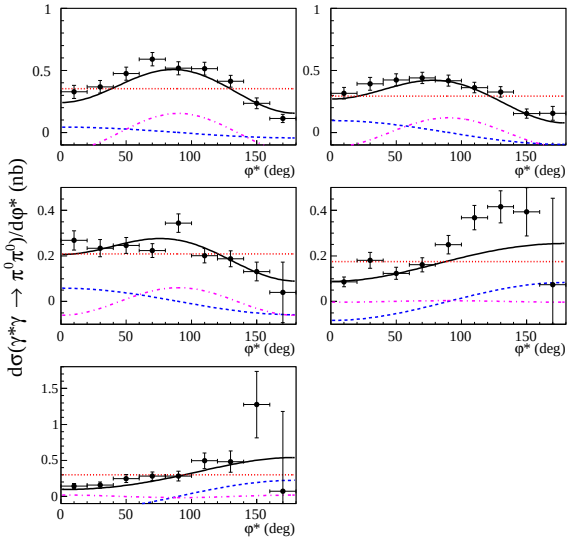

FIG. 25: φ^* dependence in five $|\cos\theta^*|$ bins: 0.1, 0.3, 0.5, 0.7, and 0.9 from left to right and top to bottom and fitted results of φ^* nominal fit. The lines are defined in Fig. 24.

The r_1 fit with $B_{D2} \neq 0$ (also with $B_{D2} = 0$) gives a unique solution as summarized in Table X. In the D_0 fit, two solutions each are obtained for both $B_{D2} \neq 0$ and $B_{D2} = 0$ as also summarized in Table X. In the D_1 fit with $B_{D2} \neq 0$, no solutions are obtained, *i.e.*, all solutions have one or more powers beyond the limit. Also, in the D_1 fit with $B_{D2} = 0$, two solutions were found with $\chi^2_{\rm P,min}/ndf = 719.7/504$, which is much worse compared to that of the D_0 fit.

As a result, it is apparent that there is a significant helicity-0 component of the $f_2(1270)$ in two-photon production when one of the photons is highly virtual. The results obtained in the φ^*-dependent fit that B_{D2} is non-zero and r_1 is non-zero are also strongly supported by the φ^*-integrated fit. The results of the r_1 fit with $B_{D2} \neq 0$ (denoted as the "r_1 nominal fit") give a unique solution with the minimum $\chi^2_{\rm P}$ and are shown in Figs. 28 – 33. Figures 28 – 32 show the angular dependence in selected W bins in each Q^2 bin while Fig. 33 shows the integrated cross section in each Q^2 bin.

To test the contribution of the $f_0(980)$, we perform a fit in which the $f_0(980)$-TFF is set to zero. This results in $\chi^2_{\rm P}/ndf = 650.2/511$ to be compared to 572.4/501 for the r_1 nominal fit. The significance of the $f_0(980)$ contribution is 7.1σ. This strongly supports the signature of the $f_0(980)$ and the validity of its TFF measurement.

E. Estimation of systematic uncertainties of TFFs

In this subsection, we estimate the systematic uncertainties for the TFFs of the $f_0(980)$ and $f_2(1270)$. They can be divided in two: the overall normalization uncertainty that affects all Q^2 bins simultaneously and the individual uncertainties that vary in each Q^2 bin. The former arises from the uncertainty of $\Gamma_{\gamma\gamma}$ and amounts to $\pm$ 6% for the $f_2(1270)$ and $\pm$ 11% for the $f_0(980)$, respectively.

Individual uncertainties are estimated in each Q^2 bin for the $f_2(1270)$-TFF, r_0, and $f_0(980)$-TFF. The individual uncertainties considered include those related to the differential cross section: normalization and distortion. The normalization uncertainty n in each bin of $|\cos\theta^*|$, W, and Q^2 varies between 0.104 and 0.253; the systematic uncertainty from this source is estimated by multiplying the cross section by the factor $1 \pm n$. The systematic uncertainties from distortion are estimated in each bin by multiplying the cross section: in W by the factor $1 \pm 0.10(W - 1.1$ GeV) ($\pm$4% distortion in the full range) and in $|\cos\theta^*|$ by the fac-

TABLE X: Fitted parameters of the φ^*-integrated cross section, where TFF parameters, $F_{f2}(Q^2)$, $r_0(Q^2)$, and $F_{f0}(Q^2)$, are obtained at each Q^2 bin (in GeV^2).

Parameter	r_1 fit		D_0 fit			
	$B_{D2}\neq 0$	$B_{D2}=0$	$B_{D2}\neq 0$		$B_{D2}=0$	
			Sol.1	Sol.2	Sol.1	Sol.2
$\chi^2_{\rm P}/ndf$	572.4/501	689.9/505	589.2/502	591.0/502	621.2/506	622.1/506
$F_{f2}(0.0);(\times 10^{-2})$	100 ± 6 (def.)					
$F_{f2}(3.5);(\times 10^{-2})$	11.5 ± 1.2	$12.6^{+1.3}_{-1.2}$	$10.9^{+1.6}_{-1.5}$	11.6 ± 1.5	$13.6^{+1.5}_{-1.4}$	$13.3^{+1.3}_{-1.3}$
$F_{f2}(4.5);(\times 10^{-2})$	$7.2^{+0.7}_{-0.8}$	7.0 ± 0.4	$7.0^{+1.2}_{-0.9}$	7.6 ± 1.0	7.5 ± 0.5	7.6 ± 0.5
$F_{f2}(5.5);(\times 10^{-2})$	$5.9^{+0.5}_{-0.6}$	5.8 ± 0.4	$5.5^{+1.0}_{-0.8}$	$6.0^{+0.9}_{-0.8}$	6.6 ± 0.4	6.5 ± 0.4
$F_{f2}(7.0);(\times 10^{-2})$	$5.1^{+0.3}_{-0.4}$	4.8 ± 0.3	$4.8^{+0.8}_{-0.7}$	$5.2^{+0.7}_{-1.4}$	5.8 ± 0.3	5.7 ± 0.3
$F_{f2}(9.0);(\times 10^{-2})$	$4.0^{+0.3}_{-0.4}$	3.8 ± 0.2	$3.8^{+0.7}_{-0.6}$	$4.1^{+0.6}_{-1.2}$	4.4 ± 0.2	4.3 ± 0.2
$F_{f2}(11.0);(\times 10^{-2})$	$3.3^{+0.3}_{-0.4}$	3.0 ± 0.2	$3.0^{+0.6}_{-0.5}$	$3.3^{+0.6}_{-1.1}$	3.6 ± 0.3	3.4 ± 0.3
$F_{f2}(13.5);(\times 10^{-2})$	2.5 ± 0.3	$2.5^{+0.3}_{-0.2}$	$2.7^{+0.5}_{-0.4}$	2.9 ± 0.5	3.4 ± 0.3	3.3 ± 0.3
$F_{f2}(17.5);(\times 10^{-2})$	2.3 ± 0.3	2.3 ± 0.3	2.2 ± 0.4	$2.4^{+0.4}_{-0.5}$	2.9 ± 0.2	2.8 ± 0.3
$F_{f2}(25.0);(\times 10^{-2})$	1.8 ± 0.2	1.4 ± 0.2	1.8 ± 0.3	2.0 ± 0.4	2.5 ± 0.2	$1.6^{+1.2}_{-0.2}$
$\phi_{f2}(^\circ)$	64^{+14}_{-32}	–	5^{+53}_{-46}	32^{+30}_{-89}	–	
$r_0(3.5);(\%)$	$45.1^{+21.8}_{-22.1}$	$51.0^{+14.9}_{-16.5}$	$37.0^{+18.4}_{-18.1}$	$33.5^{+16.7}_{-14.9}$	$56.6^{+12.0}_{-14.2}$	$52.9^{+12.1}_{-13.8}$
$r_0(4.5);(\%)$	$37.6^{+26.3}_{-15.1}$	$2.0^{+4.9}_{-2.0}$	$17.8^{+11.7}_{-8.5}$	$15.8^{+10.0}_{-7.1}$	$11.7^{+7.8}_{-6.5}$	$10.3^{+7.3}_{-5.9}$
$r_0(5.5);(\%)$	$41.7^{+15.2}_{-14.0}$	$13.8^{+8.9}_{-7.5}$	$28.0^{+13.7}_{-10.7}$	$25.6^{+12.3}_{-9.1}$	$31.2^{+8.7}_{-9.1}$	$28.8^{+8.6}_{-8.7}$
$r_0(7.0);(\%)$	$46.3^{+12.9}_{-12.1}$	$6.1^{+6.3}_{-4.6}$	$24.6^{+11.8}_{-9.0}$	$22.5^{+10.6}_{-7.4}$	$31.4^{+7.7}_{-8.2}$	$28.5^{+7.9}_{-8.2}$
$r_0(9.0);(\%)$	$35.8^{+14.0}_{-11.8}$	$4.7^{+5.4}_{-3.7}$	$21.4^{+11.9}_{-8.8}$	$20.3^{+10.9}_{-7.7}$	$21.8^{+7.5}_{-7.2}$	$18.9^{+7.4}_{-6.8}$
$r_0(11.0);(\%)$	$26.2^{+17.1}_{-14.2}$	$7.5^{+8.1}_{-5.6}$	$21.1^{+15.2}_{-10.9}$	$20.7^{+13.6}_{-9.4}$	$28.3^{+9.9}_{-10.4}$	$22.5^{+11.1}_{-10.7}$
$r_0(13.5);(\%)$	71.3 ± 19.3	$10.9^{+10.6}_{-8.2}$	$52.5^{+20.0}_{-18.1}$	$40.2^{+18.1}_{-14.3}$	$47.9^{+12.1}_{-13.2}$	$43.0^{+12.8}_{-13.8}$
$r_0(17.5);(\%)$	$53.8^{+21.8}_{-21.0}$	$26.0^{+13.5}_{-13.2}$	$44.5^{+21.8}_{-18.1}$	$37.7^{+19.9}_{-14.7}$	$55.6^{+9.9}_{-11.1}$	$52.6^{+11.0}_{-13.2}$
$r_0(25.0);(\%)$	75.3 ± 24.5	0.1 ± 4.3	$59.9^{+21.6}_{-23.0}$	$49.7^{+21.4}_{-18.6}$	$62.4^{+10.6}_{-12.9}$	3.7 ± 7.7
$\phi_{f2D0}(^\circ)$	59^{+10}_{-11}	296^{+10}_{-11}	359 ± 10	348^{+28}_{-7}	300^{+6}_{-7}	304^{+5}_{-6}
d in $r_1(Q^2)$	-0.2 ± 0.3	0.00 ± 0.04	–	–	–	–
$F_{f0}(0.0);(\times 10^{-2})$	100 ± 11 (def.)					
$F_{f0}(3.5);(\times 10^{-2})$	$18.6^{+8.1}_{-8.4}$	$11.8^{+7.0}_{-7.1}$	$16.2^{+8.4}_{-11.8}$	$15.7^{+8.3}_{-10.8}$	$10.9^{+7.2}_{-7.8}$	$11.5^{+7.2}_{-7.8}$
$F_{f0}(4.5);(\times 10^{-2})$	7.6 ± 4.9	$3.8^{+2.7}_{-3.0}$	$8.7^{+4.0}_{-6.2}$	$8.3^{+3.9}_{-5.6}$	3.0 ± 3.2	3.4 ± 3.2
$F_{f0}(5.5);(\times 10^{-2})$	8.8 ± 2.2	$3.0^{+1.9}_{-2.1}$	$7.8^{+2.4}_{-2.6}$	$7.8^{+2.3}_{-2.4}$	$2.9^{+2.1}_{-2.4}$	$3.2^{+2.1}_{-2.4}$
$F_{f0}(7.0);(\times 10^{-2})$	7.4 ± 1.5	3.0 ± 1.1	7.2 ± 1.5	$7.2^{+1.4}_{-1.4}$	3.6 ± 1.1	3.7 ± 1.1
$F_{f0}(9.0);(\times 10^{-2})$	4.7 ± 1.5	2.1 ± 0.9	$5.2^{+1.4}_{-1.5}$	$5.1^{+1.4}_{-1.5}$	2.8 ± 1.0	2.7 ± 1.0
$F_{f0}(11.0);(\times 10^{-2})$	$7.4^{+1.2}_{-1.2}$	4.0 ± 0.9	7.4 ± 1.1	7.3 ± 1.1	4.8 ± 0.9	4.6 ± 0.9
$F_{f0}(13.5);(\times 10^{-2})$	$5.4^{+1.2}_{-1.4}$	2.3 ± 0.8	5.5 ± 1.1	$5.5^{+1.1}_{-1.2}$	3.2 ± 0.8	3.0 ± 0.8
$F_{f0}(17.5);(\times 10^{-2})$	3.9 ± 1.0	0.7 ± 0.8	$3.3^{+1.0}_{-1.2}$	$3.4^{+1.0}_{-1.1}$	1.8 ± 0.9	1.3 ± 0.9
$F_{f0}(25.0);(\times 10^{-2})$	$3.5^{+0.8}_{-0.9}$	1.0 ± 0.8	$3.1^{+0.9}_{-1.0}$	$3.3^{+0.8}_{-0.9}$	1.9 ± 0.8	$1.4^{+0.8}_{-0.9}$
$\phi_{f0}(^\circ)$	23 ± 10	342^{+14}_{-16}	30^{+9}_{-10}	28^{+9}_{-10}	356^{+11}_{-12}	357^{+11}_{-12}
$a_S(\sqrt{\rm nb})$	$2.1^{+0.5}_{-0.4}$	1.8 ± 0.3	$2.4^{+0.5}_{-0.4}$	$2.4^{+0.4}_{-0.3}$	2.1 ± 0.3	2.0 ± 0.3
b_S	1.1 ± 0.2	1.8 ± 0.2	0.8 ± 0.2	$0.8^{+0.5}_{-0.1}$	1.5 ± 0.1	1.5 ± 0.1
c_S	0.6 ± 0.1	0.5 ± 0.1	0.6 ± 0.1	0.5 ± 0.1	0.5 ± 0.1	0.5 ± 0.1
$a_{D0}(\sqrt{\rm nb})$	0.2 ± 0.1	$0.5^{+0.1}_{0.0}$	$0.2^{+0.4}_{-0.1}$	$0.2^{+0.8}_{-0.1}$	$0.7^{+0.6}_{-0.4}$	0.4 ± 0.1
b_{D0}	$-1.3^{+1.3}_{-1.1}$	$-0.7^{+0.4}_{-0.4}$	-0.3 ± 1.1	$1.7^{+1.6}_{-4.3}$	$-2.2^{+1.2}_{-1.6}$	$-1.6^{+0.7}_{-0.8}$
c_{D0}	0.0 ± 1.0	0.0 ± 0.1	$0.0^{+0.4}_{-0.4}$	0.0 ± 0.8	0.4 ± 0.3	0.0 ± 0.1
$\phi_{D0}(^\circ)$	93^{+9}_{-10}	271^{+4}_{-4}	57^{+16}_{-19}	95^{+8}_{-77}	265^{+8}_{-10}	272 ± 5
$a_{D2}(\sqrt{\rm nb})$	$0.8^{+0.6}_{-0.4}$	0 (fixed)	$0.5^{+0.3}_{-0.2}$	$0.4^{+0.3}_{-0.2}$	0 (fixed)	0 (fixed)
b_{D2}	$0.3^{+1.2}_{-1.2}$	0 (fixed)	$2.1^{+0.5}_{-0.9}$	$-0.9^{+3.8}_{-1.4}$	0 (fixed)	0 (fixed)
c_{D2}	0.3 ± 0.3	0 (fixed)	0.2 ± 0.2	0.2 ± 0.1	0 (fixed)	0 (fixed)

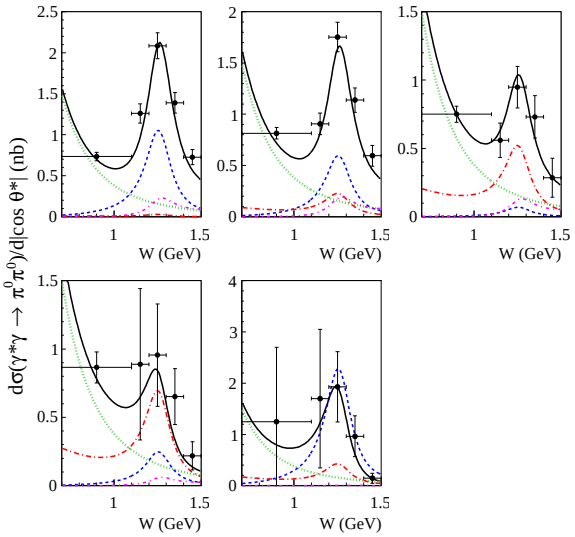

FIG. 26: W dependence in five $|\cos\theta^*|$ bins: 0.1, 0.3, 0.5, 0.7, and 0.9 from left to right and top to bottom and fitted results of φ^* nominal fit. The lines are defined in Fig. 23.

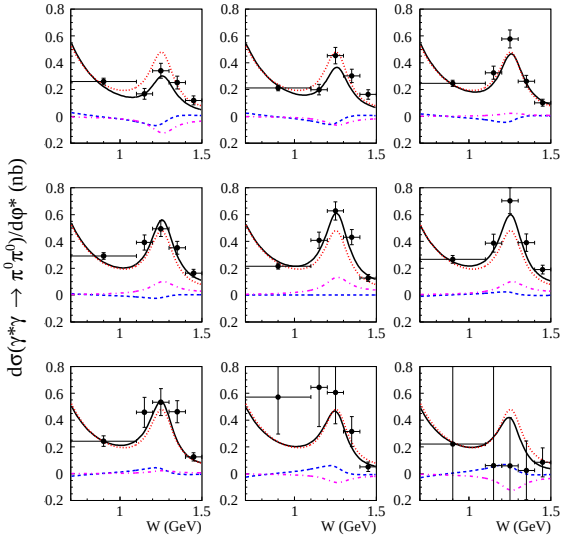

FIG. 27: W dependence in nine φ^* bins: 10° to 170° in 20° step from left to right and top to bottom and fitted results of φ^* nominal fit. The lines are defined in Fig. 24.

tor $1 \mp [(a+b)|\cos\theta^*| - a]$, where a (b) has values $0.01 - 0.09$ ($0.02 - 0.16$) depending on W and Q^2 ($^{+a}_{-b}$ or $^{-a}_{+b}$ distortion in the full range). The values of n, a, b are estimated in Sec. VI F. The other individual uncertainties considered are from the fitted W range, from the parameterization and from assumed constants. The fitted W ranges are changed to $0.65 - 1.4$ GeV or to $0.75 - 1.6$ GeV. The parameterization of the background B_i is changed to $W/(1.1 \pm 0.2)$ GeV or to $Q^2/(1.0 \pm 0.5)$ GeV^2. We also set $B_1 \neq 0$ to study its effect. The properties of the $f_0(980)$ and $f_2(1270)$ are changed using the world-average values [34]. Also r_R in the $f_2(1270)$ parameterization is varied by its error. We have also taken into account the uncertainty of $r_1(Q^2_{\rm av})$ obtained in the φ^*-dependent analysis, which is evaluated by setting the distortion of $\pm 4\%$ in φ^*. The estimated systematic uncertainty of $r_1(Q^2_{\rm av})$ is much smaller than the statistical uncertainties obtained in the fit. Thus, we set $r_1(Q^2_{\rm av}) = 0.15 \pm 0.05$. A shift of the $f_0(980)$ mass ((980 ± 20) MeV$/c^2$) gives rise to a large effect due to its proximity to the $K\bar{K}$ threshold. All the uncertainties are summed in quadrature in each Q^2 bin. For the $f_2(1270)$-TFF, systematic uncertainties for the helicity-0, -1, and -2 components are calculated from the values of $f_2(1270)$-TFF, r_0, and d in r_1 (Eq. (43)). The results are summarized in Table XI.

F. Q^2 dependence of TFFs for the $f_2(1270)$ and $f_0(980)$

The obtained Q^2 dependence of TFF for the $f_2(1270)$ for the r_1 nominal fit is shown in Fig. 34 for the helicity-2 component. Also shown are the predicted Q^2 dependence by Ref. [4] and those from Ref. [5] (Eqs. (1) and (2)). The theoretical prediction of Ref. [4] and of Eq. (2) in Ref. [5] agree well with data.

Figure 35 (36) shows the helicity-0 (helicity-1) TFF obtained for the $f_2(1270)$ together with the prediction [4]. Note that the helicity-1 TFF is calculated from $\sqrt{r_1(Q^2)}F_{f2}(Q^2)$, where $r_1(Q^2)$ is given by Eq. (43). The measured value calculated from r_0 at $Q^2 = 0$, $r_0(0) = (3.56^{+0.22+12.81}_{-0.27-2.74})\%$ [28], is also plotted in Fig. 35, while Ref. [4] predicts zero at $Q^2 = 0$ (Table I). The first and second errors of $r_0(0)$ are statistical and systematic, respectively. The prediction is a factor of $1.5 - 2$ larger than the measured values.

Figure 37 shows the obtained Q^2 dependence of the TFF of the $f_0(980)$ for the r_1 nominal fit. Here, the theoretical prediction for a scalar TFF in Ref. [4] agrees well with the measured ones up to $Q^2 \simeq 10$ GeV^2 but has steeper Q^2 dependence for $Q^2 > 10$ GeV^2.

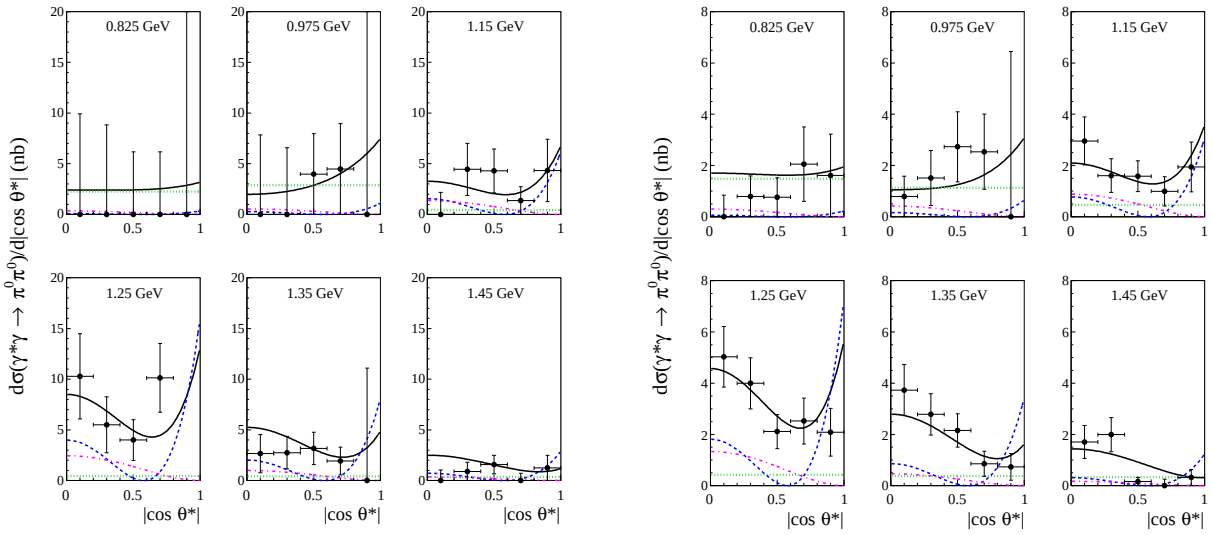

FIG. 28: Angular dependence of the cross section in the indicated W bin and results of the r_1 fit at $Q^2 = 3.5$ GeV^2 (left) and $Q^2 = 4.5$ GeV^2 (right). Legend of lines: solid lines for the total (black), dotted $|S|^2$ (green), dashed $|D_0|^2$ (blue), and dash-dotted $|D_2|^2$ (purple).

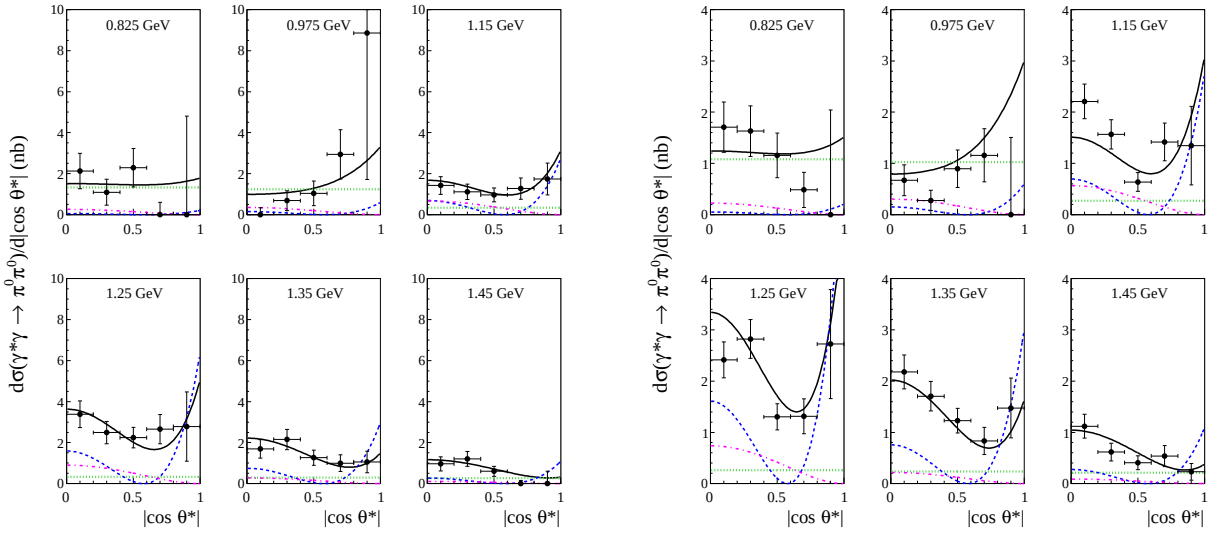

FIG. 29: Angular dependence of the cross section in the indicated W bin and results of the r_1 fit at $Q^2 = 5.5$ GeV^2 (left) and $Q^2 = 7.0$ GeV^2 (right). The lines are defined in Fig. 28.

VIII. SUMMARY AND CONCLUSIONS

We have measured for the first time the differential cross section of π^0 pair production in single-tag two-photon collisions, $\gamma^*\gamma \to \pi^0\pi^0$ up to $Q^2 = 30$ GeV^2 based on a data sample of 759 fb^{-1} collected with the Belle detector [15, 16] at the KEKB asymmetric-energy e^+e^- collider [17]. The kinematical range of the data is 0.5 GeV $< W <$ 2.1 GeV and $|\cos\theta^*| <$ 1.0 in the $\gamma^*\gamma$ center-of-mass system.

The azimuthal angle dependence shows that the contribution of the helicity-0 (helicity-1) component of the $f_2(1270)$ is large (small but non-zero). The differential cross section is fitted by parameterizing partial-wave amplitudes. The transition form factors

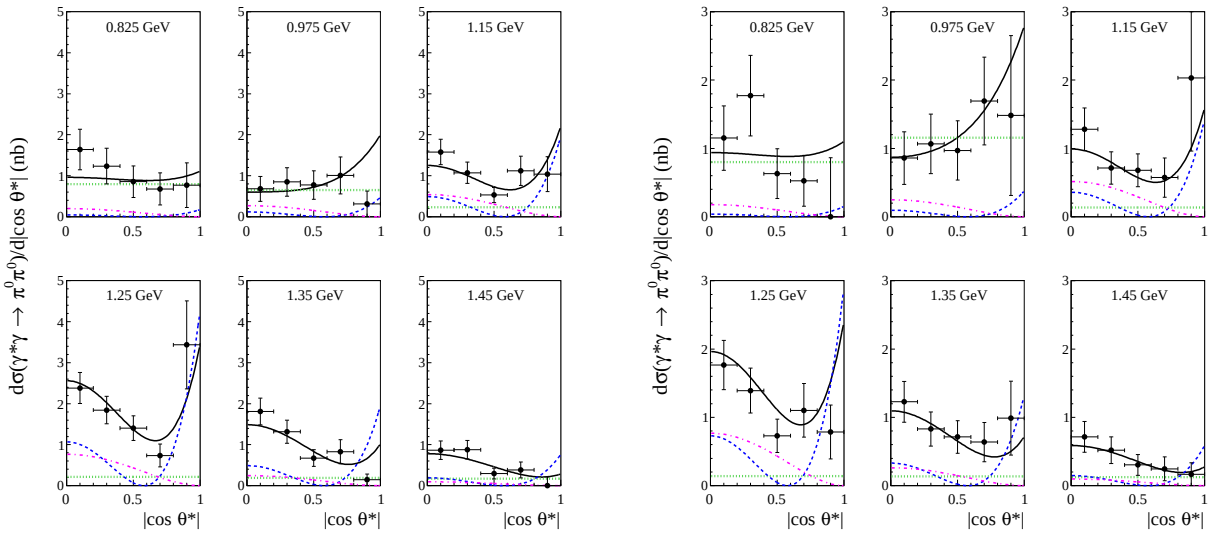

FIG. 30: Angular dependence of the cross section in the indicated W bin and results of the r_1 fit at $Q^2 = 9.0$ GeV^2 (left) and $Q^2 = 11.0$ GeV^2 (right). The lines are defined in Fig. 28.

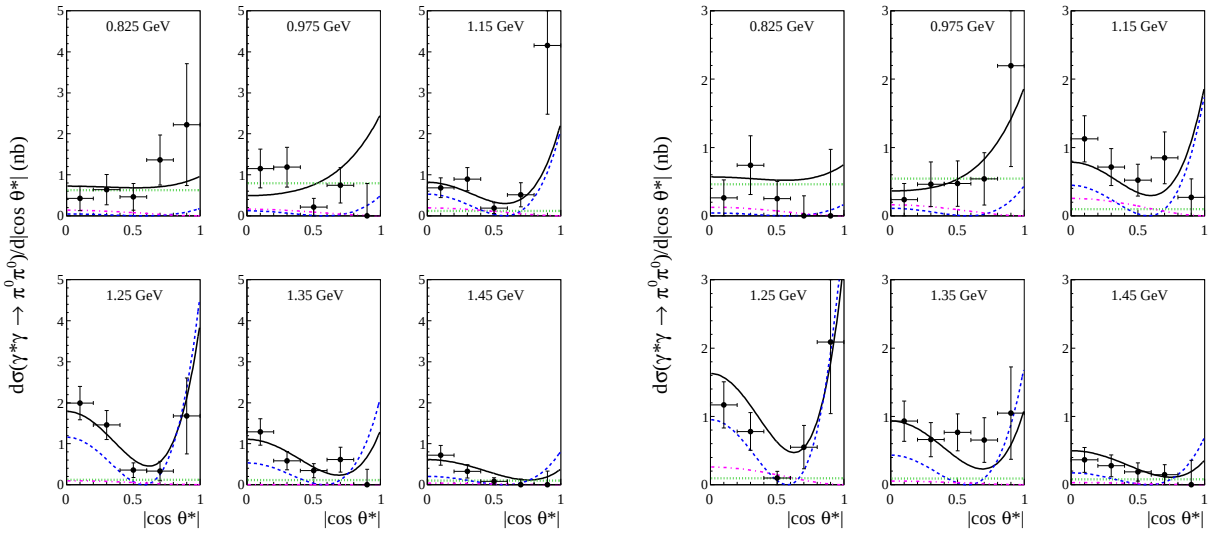

FIG. 31: Angular dependence of the cross section in the indicated W bin and results of the r_1 fit at $Q^2 = 13.5$ GeV^2 (left) and $Q^2 = 17.5$ GeV^2 (right). The lines are defined in Fig. 28.

of the $f_2(1270)$ and $f_0(980)$ are measured for Q^2 up to 30 GeV^2 and compared with theoretical predictions. For the $f_2(1270)$, the helicity-0, -1, and -2 TFFs are measured. The measured helicity-2 TFF of the $f_2(1270)$ agrees well with the theory prediction of Ref. [4] and with one of the two predictions in Ref. [5]. The helicity-0 and -1 TFF are about a factor of $1.5 - 2$ smaller than the prediction of Ref. [4].

The TFF of the $f_0(980)$ is also extracted; the resulting Q^2 dependence agrees fairly well with the prediction of Ref. [4] for $Q^2 \leq 10$ GeV^2 but has less steeper Q^2 dependence for $Q^2 > 10$ GeV^2.

TABLE XI: Resulting transition form factors for the $f_0(980)$ and $f_2(1270)$ ($\times 10^{-2}$). The first and second errors are statistical and systematic, respectively.

$\bar{Q}^2$	$f_0(980)$-TFF	$f_2(1270)$-TFF			
		Hel. = 0	Hel. = 1	Hel. = 2	Total
0	100 (def.)	$18.9^{+0.6+21.6}_{-0.7-9.8}$	–	$98.2 \pm 0.1^{+1.4}_{-6.5}$	100 (def.)
3.45	$18.7^{+8.1+5.6}_{-8.4-2.0}$	$7.7^{+2.0+2.4}_{-2.1-0.8}$	$5.0 \pm 0.9^{+0.9}_{-0.5}$	$7.2 \pm 2.2^{+0.8}_{-2.6}$	$11.5 \pm 1.2 \pm 1.0$
4.46	$7.6^{+4.9+4.2}_{-4.9-0.6}$	$4.4^{+1.6+0.6}_{-1.0-1.6}$	$3.1^{+0.4+0.5}_{-0.5-0.9}$	$4.9^{+0.9+1.1}_{-1.5-1.6}$	$7.2^{+0.7+0.9}_{-0.8-2.2}$
5.47	$8.8 \pm 2.2^{+3.3}_{-1.0}$	$3.8 \pm 0.8^{+1.1}_{-0.9}$	$2.5 \pm 0.3^{+0.4}_{-0.5}$	$3.9^{+0.7+0.6}_{-0.8-1.3}$	$5.9^{+0.5+0.7}_{-0.6-1.2}$
6.89	$7.4 \pm 1.5^{+2.3}_{-0.8}$	$3.5^{+0.6+0.9}_{-0.5-0.7}$	$2.1 \pm 0.2^{+0.3}_{-0.4}$	$3.2 \pm 0.6^{+0.5}_{-1.1}$	$5.1^{+0.3+0.6}_{-0.4-0.9}$
8.92	$4.5 \pm 1.5^{+1.2}_{-0.5}$	$2.4 \pm 0.5 \pm 0.7$	$1.6^{+0.1+0.2}_{-0.2-0.4}$	$2.8^{+0.4+0.4}_{-0.5-1.0}$	$4.0^{+0.3+0.5}_{-0.4-1.1}$
10.93	$7.4 \pm 1.2^{+1.8}_{-0.7}$	$1.7^{+0.6+1.4}_{-0.5-0.5}$	$1.3 \pm 0.1^{+0.1}_{-0.3}$	$2.5^{+0.4+0.3}_{-0.5-1.1}$	$3.3^{+0.3+0.4}_{-0.4-0.8}$
13.37	$5.4^{+1.2+0.9}_{-1.4-0.6}$	$2.1 \pm 0.4^{+0.4}_{-0.2}$	$0.9 \pm 0.1^{+0.2}_{-0.1}$	$0.9 \pm 0.7^{+0.3}_{-0.4}$	$2.5 \pm 0.3^{+0.5}_{-0.2}$
17.23	$3.9 \pm 1.0^{+1.0}_{-0.5}$	$1.7 \pm 0.4^{+0.6}_{-0.2}$	$0.8 \pm 0.1 \pm 0.1$	$1.3 \pm 0.5^{+0.3}_{-0.8}$	$2.3 \pm 0.3^{+0.3}_{-0.2}$
24.25	$3.5^{+0.8+0.7}_{-0.9-0.5}$	$1.6 \pm 0.3^{+0.3}_{-0.2}$	$0.6 \pm 0.1 \pm 0.1$	$0.6 \pm 0.7^{+0.4}_{-0.5}$	$1.8 \pm 0.2^{+0.4}_{-0.1}$

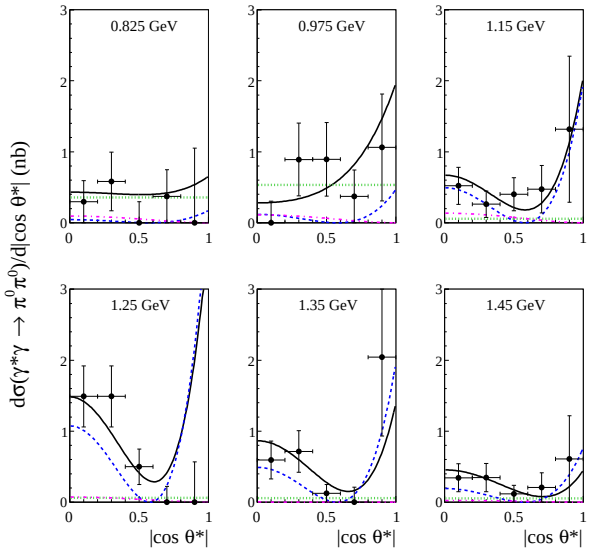

FIG. 32: Angular dependence of the cross section in the indicated W bin and results of the r_1 fit at $Q^2 = 25$ GeV^2. The lines are defined in Fig. 28.

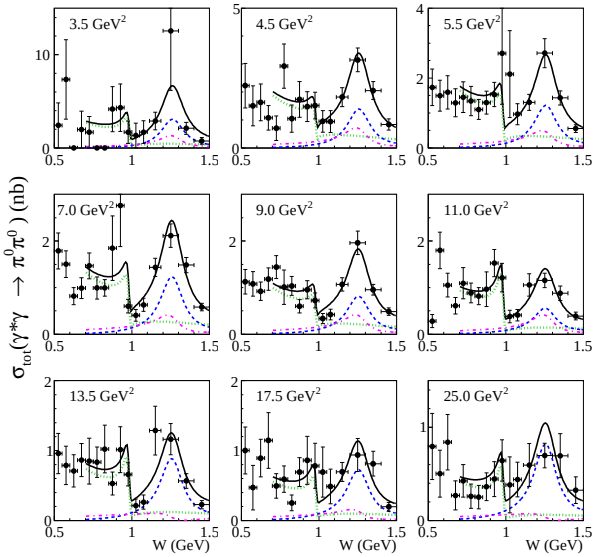

FIG. 33: Integrated cross section in the indicated Q^2 bin and results of the r_1 fit. The lines are defined in Fig. 28.

Acknowledgments

Special thanks are due to V.G. Serbo for various useful discussions and for kindly providing the cross section formula that includes the φ^* dependence for single-tag two-photon production of $\pi^0\pi^0$, without which we could not perform this analysis.

We thank the KEKB group for the excellent operation of the accelerator; the KEK cryogenics group for the efficient operation of the solenoid; and the KEK computer group, the National Institute of Informatics, and the PNNL/EMSL computing group for valuable computing and SINET4 network support. We acknowledge support from the Ministry of Education, Culture, Sports, Science, and Technology (MEXT) of Japan, the Japan Society for the Promotion of Science (JSPS), and the Tau-Lepton Physics Research Center of Nagoya University; the Australian Research Council and the Australian Department of Industry, Innovation, Science and Research; Austrian Science Fund under Grant No. P 22742-N16 and P 26794-N20; the National Natural Science Foundation of China under Contracts No. 10575109, No. 10775142, No. 10875115, No. 11175187, and

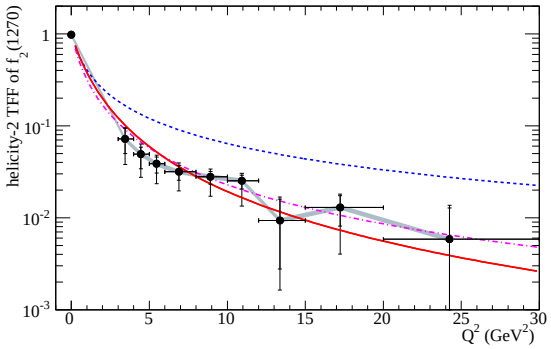

FIG. 34: The measured helicity-2 TFF of the $f_2(1270)$ as a function of Q^2. Short (long) vertical bars indicate statistical (statistical and systematic combined) errors. The shaded area corresponds to the overall systematic uncertainty arising from that of $\Gamma_{\gamma\gamma}$. Correlations of uncertainties between neighboring bins exist and are included in the long vertical bars. The solid line shows the predicted Q^2 dependence in Table I by Ref. [4] and those by Ref. [5]: Eq. (1) (dashed line) and Eq. (2) (dot-dashed line). The theoretical curves for the helicity-2 TFF are normalized to 1 at $Q^2 = 0$.

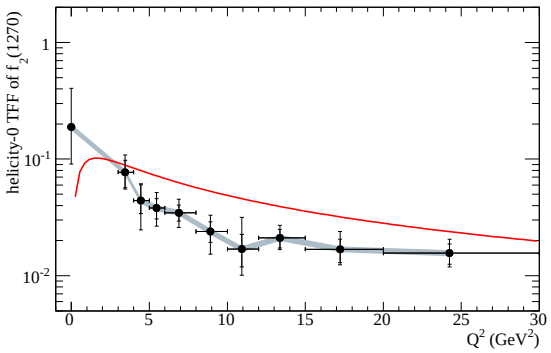

FIG. 35: The measured helicity-0 TFF of the $f_2(1270)$ as a function of Q^2. Short (long) vertical bars indicate statistical (statistical and systematic combined) errors. The shaded area corresponds to the overall systematic uncertainty arising from that of $\Gamma_{\gamma\gamma}$. Correlations of uncertainties between neighboring bins exist and are included in the long vertical bars. The solid line shows the predicted Q^2 dependence in Table I by Ref. [4].

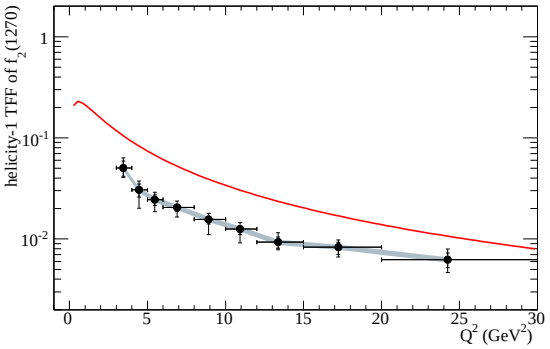

FIG. 36: The measured helicity-1 TFF of the $f_2(1270)$ as a function of Q^2. Short (long) vertical bars indicate statistical (statistical and systematic combined) errors. The shaded area corresponds to the overall systematic uncertainty arising from that of $\Gamma_{\gamma\gamma}$. Correlations of uncertainties between neighboring bins exist and are included in the long vertical bars. Note that the helicity-1 TFF is calculated from $\sqrt{r_1(Q^2)}F_{f2}(Q^2)$, where $r_1(Q^2)$ is given by Eq. (43). The solid line shows the predicted Q^2 dependence in Table I by Ref. [4].

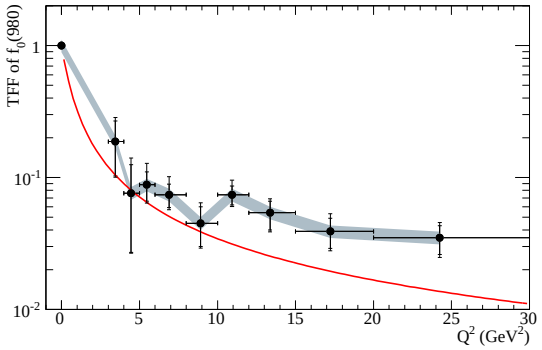

FIG. 37: The measured Q^2 dependence of the TFF of the $f_0(980)$. Short (long) vertical bars indicate statistical (statistical and systematic combined) errors. The shaded area corresponds to the overall systematic uncertainty arising from that of $\Gamma_{\gamma\gamma}$. Correlations of uncertainties between neighboring bins exist and are included in the long vertical bars. The solid curve is the prediction for a scalar particle given in Table I by Ref. [4].

No. 11475187; the Chinese Academy of Science Center for Excellence in Particle Physics; the Ministry of Education, Youth and Sports of the Czech Republic under Contract No. LG14034; the Carl Zeiss Foundation, the Deutsche Forschungsgemeinschaft and the VolkswagenStiftung; the Department of Science and Technology of India; the Istituto Nazionale di Fisica Nucleare of Italy; National Research Foundation (NRF) of Korea Grants No. 2011-0029457, No. 2012-0008143, No. 2012R1A1A2008330, No. 2013R1A1A3007772, No. 2014R1A2A2A01005286, No. 2014R1A2A2A01002734, No. 2014R1A1A2006456; the Basic Research Lab program under NRF Grant No. KRF-2011-

0020333, No. KRF-2011-0021196, Center for Korean J-PARC Users, No. NRF-2013K1A3A7A06056592; the Brain Korea 21-Plus program and the Global Science Experimental Data Hub Center of the Korea Institute of Science and Technology Information; the Polish Ministry of Science and Higher Education and the National Science Center; the Ministry of Education and Science of the Russian Federation and the Russian Foundation for Basic Research; the Slovenian Research Agency; the Basque Foundation for Science (IKERBASQUE) and the Euskal Herriko Unibertsitatea (UPV/EHU) under program UFI 11/55 (Spain); the Swiss National Science Foundation; the National Science Council and the Ministry of Education of Taiwan; and the U.S. Department of Energy and the National Science Foundation. This work is supported by a Grant-in-Aid from MEXT for Science Research in a Priority Area ("New Development of Flavor Physics") and from JSPS for Creative Scientific Research ("Evolution of Tau-lepton Physics").

REFERENCES

[1] M. Diehl, T. Gousset, B. Pire and O. Teryaev, Phys. Rev. Lett. **81**, 1782 (1998); M. Diehl, T. Gousset and B. Pire, Phys. Rev. D **62**, 073014 (2000).

[2] V. M. Braun and N. Kivel, Phys. Lett. B **501**, 48 (2001).

[3] G. Colangelo, M. Hoferichter, M. Procura and P. Stoffer, J. High Energy Physics **1409**, 091 (2014); G. Colangelo, M. Hoferichter, B. Kubis, M. Procura and P. Stoffer, Phys. Lett. B **738**, 6 (2014).

[4] G.A. Schuler, F.A. Berends and R. van Gulik, Nucl. Phys. B **523**, 423 (1998).

[5] V. Pascalutsa, V. Pauk and M. Vanderhaeghen, Phys. Rev. D **85**, 116001 (2012).

[6] J. Gronberg *et al.* (CLEO Collaboration), Phys. Rev. D **57**, 33 (1998).

[7] P. Achard *et al.* (L3 Collaboration), Phys. Lett. B **526**, 269 (2002).

[8] P. Achard *et al.* (L3 Collaboration), J. High Energy Phys. **03**, 018 (2007).

[9] B. Aubert *et al.* (BaBar Collaboration), Phys. Rev. D **80**, 052002 (2009).

[10] S. Uehara *et al.* (Belle Collaboration), Phys. Rev. D **86**, 092007 (2012).

[11] P. del Amo Sanchez *et al.* (BaBar Collaboration), Phys. Rev. D **84**, 052001 (2011).

[12] J.P. Lees *et al.* (BaBar Collaboration), Phys. Rev. D **81**, 052010 (2010).

[13] H. Aihara *et al.* (TPC/Two-Gamma Collaboration), Phys. Rev. Lett. **57**, 404 (1986).

[14] I.F. Ginzburg, A. Schiller and V.G. Serbo, Eur. Phys. J, C **18**, 731 (2001); and private communication with V.G. Serbo.

[15] A. Abashian *et al.* (Belle Collaboration), Nucl. Instr. and Meth. A **479**, 117 (2002).

[16] J. Brodzicka *et al.* (Belle Collaboration), Prog. Theor. Exp. Phys. 2012, 04D001 (2012).

[17] S. Kurokawa and E. Kikutani, Nucl. Instr. and Meth. A **499**, 1 (2003), and other papers included in this volume; T. Abe *et al.*, Prog. Theor. Exp. Phys. 2013, 03A001 (2013).

[18] B.G. Cheon *et al.*, Nucl. Instr. and Meth. A **494**, 548 (2002).

[19] Ch. Berger and W. Wagner, Phys. Rep. **146**, 1 (1987).

[20] S. Uehara, KEK Report 96-11 (1996), arXiv:1310.0157 [hep-ph]

[21] G.A. Schuler, CERN-TH/96-297, arXiv:hep-ph/9610406 (1996).

[22] E. Etim, G. Pancheri and B. Touschek, Nuovo Cimento **51** B, 276 (1967).

[23] V.P. Druzhinin, L.V. Kardapoltsev and V.A. Tayursky, Comp. Phys. Commun. **185**, 236 (2014); S. Ong and P. Kessler, Phys. Rev. D **38**, 2280 (1988); M. Benayoun, S.I. Eidelman, V.N. Ivanchenko and Z.K. Silagadze, Mod. Phys. Lett. A **14**, 2605 (1999); F. Jegerlehner, J. Phys. G **29**, 101 (2003); F.A. Berends, P.H. Daverveldt, R. Kleiss, Nucl. Phys B **253**, 421 (1985).

[24] R. Brun *et al.*, CERN DD/EE/84-1 (1987).

[25] T. Skwarnicki, Ph.D Thesis, DESY F31-86-02(1986), Appendix E.

[26] M. Acciarri *et al.* (L3 Collaboration), Phys. Lett. B **413**, 147 (1997).

[27] D. Antreasyan *et al.* (Crystal Ball Collaboration), Z. Phys. C **48**, 561 (1990).

[28] S. Uehara *et al.* (Belle Collaboration), Phys. Rev. D **78**, 052004 (2008).

[29] S. Uehara *et al.* (Belle Collaboration), Phys. Rev. D **79**, 052009 (2009).

[30] We denote individual partial waves by roman letters and parameterized waves by italic.

[31] T. Mori *et al.* (Belle Collaboration), Phys. Rev. D **75**, 051101(R) (2007).

[32] T. Mori *et al.* (Belle Collaboration), J. Phys. Soc. Jpn, **76**, 074102 (2007).

[33] S.M. Flatté, Phys. Lett. **63B**, 224 (1976); N.N. Achasov and G.N. Shestakov, Phys. Rev. D **72**, 013006 (2005).

[34] J. Beringer *et al.* (Particle Data Group), Phys. Rev. D **86** , 010001 (2012).

[35] M. Ablikim *et al.* (BES Collaboration), Phys. Lett. B **607**, 243 (2005).

[36] J.M. Blatt and V.F. Weisskopf, *Theoretical Nuclear Physics* (Wiley, New York, 1952), pp. 359-365 and 386-389.

[37] G. Grayer *et al.*, Nucl. Phys. B **75**, 189 (1974); A. Garmash *et al.* (Belle Collaboration), Phys. Rev. D **71**, 092003 (2005); B. Aubert *et al.* (BaBar Collaboration), Phys. Rev. D **72**, 052002 (2005).

[38] See the review by S. Baker and R.D. Cousins, Nucl. Instr. and Meth. in Phys. Res.**221**, 437 (1984).

[39] F. James and M. Roos, Comput. Phys. Commun. **10**, 343 (1975).